Unified Lagrangian formulation for solid and fluid mechanics and FSI problems

Alessandro Franci, Eugenio Oñate, Josep Maria Carbonell

Abstract

We present a Lagrangian monolithic strategy for fluid-structure interaction (FSI) problems. The formulation is called Unified because the fluid and the solid mechanics problems are solved using the same solution scheme and unknown variables. The method is based on a mixed velocity-pressure formulation. Each time step increment is solved via an iterative partitioned two-step procedure. The fluid parts of the domain are solved using the Particle Finite Element Method (PFEM), while for solids the Finite Element Method (FEM) is employed. Both the velocity and the pressure fields are interpolated using linear shape functions. For quasi-incompressible materials, the velocity-pressure formulation is stabilized with the Finite Calculus (FIC) method presented in [1]. Adapting this scheme to quasi-incompressible hypoelastic solids and Newtonian fluids, the VPS/S-element and the VPS/F-element, respectively, are derived. Other two non-stabilized elements are presented for hypoelastic solids, namely the V-element and the VP-element. The former is based on a Velocity formulation and the latter on Velocity-Pressure formulation. The algorithms for coupling solid elements with the VPS/F fluid element are explained in detail. The Unified formulation is validated by solving benchmark FSI problems and by comparing the numerical solution to the ones published in the literature.

Keywords: Unified formulation, FSI, PFEM, Lagrangian formulation, quasi-incompressible model

1. Introduction

The aim of this work is to derive a finite element formulation capable to solve the mechanics of a general continuum through a unique set of equations and unkown variables. The term 'general continuum' refers to a domain that may include compressible or quasi-incompressible solids and fluids interacting together. For this reason, the formulation is termed *Unified*.

There are many reasons for undertaking the above objective. The first advantage of the Unified formulation is that it allows to solve fluid and solid dynamics problems by implementing and using a single calculation code. Furthermore, if solids and fluids are solved via the same scheme, it is simpler to extend the solver for FSI problems because it is not required neither changing the variables, neither implementing the transfer of transmission conditions through the interface. With this formulation solids and fluids represent regions of the same continuum and they differ only by the specific values of the material parameters. As a consequence, the FSI solver requires a small implementation work. Additionally, the Unified formulation leads to a monolithic solution scheme for FSI problems. This gives the further advantage that the coupling is ensured strongly and an iteration loop is not required, differently from staggered procedures. Finally, using the same set of unknowns for the fluid and the solid domains improves the conditioning of the FSI solver, because the solution system does not include variables of different units of measure.

The Unified formulation allow us to couple a Velocity-Pressure Stabilized formulation for Fluids (VPS/F-element) with three different types of hypoelastic elements for solids, namely the V, the VP and the VPS/S elements, corresponding to a Velocity, a Velocity-Pressure and a Velocity-Pressure Stabilized formulation, respectively. The governing equations are solved using an updated Lagrangian (UL) description and via a two-step Gauss-Seidel partitioned iterative scheme. First, the momentum equations are solved for the velocity increments. Then, for the mixed elements, the continuity equation is solved for the pressure in the updated configuration using the velocities computed at the first

step.

The continuity equation is expressed considering the compressibility of the material through a term depending on the bulk modulus κ. This allow us to use the same form of the continuity equation for compressible, quasi-incompressible and fully incompressible materials. In fact, depending on the value of the bulk modulus, each of the mentioned cases can be solved. For example, for incompressible materials $\kappa = \infty$ is considered and the canonical divergence-free form of the continuity equation of the Navier-Stokes problem is recovered.

The same linear interpolation is used for the velocity and the pressure fields. It is well known that, for incompressible (or quasi-incompressible) problems, this combination does not fulfill the $inf - sup$ condition [2] and a stabilization method is required. In this work the Finite Calculus (FIC) stabilization procedure [3, 4, 5, 6, 7, 8] is used. The FIC approach in mechanics is based on expressing the equations of balance of mass and momentum in a space-time domain of finite size. In addition to the standard terms of infinitesimal theory, the FIC form of the balance equations contains derivatives of the classical differential equations in mechanics multiplied by characteristic distances in space and time. In this work, the problem is stabilized using the FIC method derived and validated in [1] for quasi-incompressible Newtonian fluids. In particular, the VPS/F-element has been implemented following precisely the scheme presented in [1].

Introducing just small modifications, the same stabilization procedure is used also by the VPS/S-element for analysis of quasi-incompressible hypoelastic solids. For solids far from the incompressible behavior, other two types of hypoelastic elements are presented, namely the V and the VP elements. The latter is based on the same scheme of the VPS/S-element, but the standard non-stabilized form is used for the continuity equation. Instead, the V-element is based on a pure velocity formulation. In this case, the stresses are computed using the velocity only and the continuity equation is not solved.

The solid parts of the domain are solved using the Finite Element Method (FEM) [9], while for the VPS/F fluid element the Particle Finite Element

Method (PFEM) [10] is used. The PFEM is a Lagrangian strategy that treats the mesh nodes of the domain as particles which can freely move and even separate from the rest of the fluid domain representing, for instance, the effect of water drops. A mesh connects the nodes discretizing the domain where the governing equations are solved using the FEM. The domain is continuously remeshed using a procedure that efficiently combines the Delaunay tesselation and the Alpha Shape Method [11]. These features make the PFEM the ideal numerical procedure to model and simulate free surface flows. In the last years, many scientific publications have shown the efficiency of the PFEM for solving free surface flow problems, [12, 13, 14]. The PFEM can be also used for other problems such as those involving thermal convection-diffusion [15, 16, 17], multi-fluids [18, 19], granular materials [20], bed erosion [21], FSI [22, 23], excavation [24, 25] or industrial forming processes [26].

The FSI problem is solved with a monolithic scheme. This means that fluids and solids are solved within the same linear system of algebraic equations. Thanks to the many analogies in the analysis of fluids and solids, the implementation work for coupling the mechanics of fluids and solids is reduced to a proper assembly of the global linear system and to the geometric detection of the fluid-solid interface.

This text is organized as follows. In the next section, the governing equations of a general continuum are introduced. Then the constitutive laws used in this work for fluids and solids, namely the hypoelastic and quasi-incompressible Newtonian models, are presented. Section 4 is devoted to the linearization of the linear momentum equations. In the following section the continuity equation is discretized. In Section 6 the FIC-stabilized form of the continuity equation is given, first for Newtonian fluids and then for quasi-incompressible hypoelastic solids. The solution scheme of the Unified formulation for solving FSI problems for a generic time step is described in Section 7. The different expressions for the VPS/F-element for fluids, the V, VP, VPS/S elements for solids are detailed. The way to assemble the global linear system and to detect the fluid-solid interface is then explained. In Section 9 some numerical examples are

given in order to validate the Unified formulation for FSI problems. Finally, the conclusions of this work are given.

2. Governing equations

The governing equations for a general continuum (either a fluid or a solid) are the linear momentum equations, with the corresponding boundary conditions, and the continuity equation. These equations are coupled with the constitutive relationships (Section). In this work, the solving equations will be written in the Updated Lagrangian (UL) formulation [27].

In order to avoid ambiguities, the variables and the matrices referred to fluids will be indentified by subindex 'f ', and those ones refered to solids by subindex 's '. When both materials may be involved, the subindex will be 's,f '.

For a general continuum, the local form of the linear momentum equations using the UL description reads [1]

$$\rho(\mathbf{X},t)\frac{\partial \mathbf{v}(\mathbf{X},t)}{\partial t} - \frac{\partial \boldsymbol{\sigma}(\mathbf{X},t)}{\partial \mathbf{x}} - \mathbf{b}(\mathbf{X},t) = 0 \qquad in\ \Omega \times (0,T) \tag{1}$$

where ρ is the density of the material, $\boldsymbol{v}$ are the velocity vector, $\boldsymbol{\sigma}$ is the Cauchy stress tensor and $\boldsymbol{b}$ is the body force vector. The variables within the brackets are the independent variables. In particular, $\mathbf{X}$ are the Lagrangian or material coordinates vector, $\mathbf{x}$ the Eulerian or spatial coordinates vector and t is the time. For simplicity, in the following the independent variables will be not specified.

The linear momentum equations are completed by the following conditions at the Dirichlet (Γ_v) and Neumann (Γ_t) boundaries

$$v_i - v_i^p = 0 \qquad \text{on } \Gamma_v \tag{2}$$

$$\sigma_{ij} n_j - t_i^p = 0 \qquad \text{on } \Gamma_t \tag{3}$$

where v_i^p and t_i^p, $i = 1, ..., n_s$ are the prescribed velocities and the prescribed tractions, respectively.

The continuity equation is written in the following general form [28]

$$\frac{1}{\kappa_{f,s}}\frac{\partial p}{\partial t} = d^v \tag{4}$$

where $\kappa_{f,s}$ is the bulk modulus for either the fluid or the solid, p is the pressure (defined positive in tension) and d^v is the volumetric strain rate which is defined as

$$d^v = d_{ii} \tag{5}$$

where $\boldsymbol{d}$ is the spatial strain rate tensor computed as a function of the velocities as

$$d_{ij} = \frac{1}{2}\left(\frac{\partial v_i}{\partial x_j} + \frac{\partial v_j}{\partial x_i}\right) \tag{6}$$

In the following, summation of terms for repeated indices is assumed, unless otherwise specified.

Note that, depending on the values of the material bulk modulus, the continuity equation in the form of Eq.(4) can be used for (standard) compressible, quasi-incompressible and fully incompressible materials, indifferently. For example, $\kappa = \infty$ yields $d_v = 0$ and canonical form of the continuity equation for incompressible materials is recovered.

3. Constitutive laws

In this work, a hypoelastic constitutive law is used for solids, while for fluids the quasi-incompressible Newtonian model is considered. In the Unified formulation the constitutive relations are expressed in the following form

$$\boldsymbol{\sigma}^{\nabla} = \boldsymbol{c}^{\nabla\sigma} : \boldsymbol{d} \tag{7}$$

where $\boldsymbol{\sigma}^{\nabla}$ is the Cauchy stress rate tensor, $\boldsymbol{c}^{\nabla\sigma}$ is the fourth-order tangent moduli tensor and $\boldsymbol{d}$ is the deformation rate tensor.

In this section, the tangent moduli for the rate of the Cauchy stress $\boldsymbol{c}^{\nabla\sigma}$ is given and the computation of the stresses is explained for both hypoelastic solids and Newtonian fluids.

3.1. Hypoelasticity

A hypoelastic body is defined by a direct relation between the rate of stress and the rate of strain [29]. Considering a isotropic body and using a Jaumann

measure of stress, the Cauchy stress rate tensor is computed as [30]

$$\boldsymbol{\sigma}^{\triangledown} = \boldsymbol{c}^{\sigma J} : \boldsymbol{d} \tag{8}$$

where the Jaumann fourth-order tangent moduli $\boldsymbol{c}^{\sigma J}$ is

$$c^{\sigma J}_{ijkl} = \kappa_s \delta_{ij}\delta_{kl} + \mu_s \left(\delta_{ik}\delta_{jl} + \delta_{il}\delta_{kj} - \frac{2}{3}\delta_{ij}\delta_{kl} \right) \quad , \quad \boldsymbol{c}^{\sigma J} = \kappa_s \boldsymbol{I} \otimes \boldsymbol{I} + 2\mu_s \mathbf{I}' \tag{9}$$

for a 2D problem, $\boldsymbol{c}^{\sigma J} = \begin{bmatrix} \kappa_s + \frac{4}{3}\mu_s & \kappa_s - \frac{2}{3}\mu_s & 0 \\ \kappa_s - \frac{2}{3}\mu_s & \kappa_s + \frac{4}{3}\mu_s & 0 \\ 0 & 0 & \mu_s \end{bmatrix}$

where κ_s is the solid bulk modulus computed from the Lamé parameters, λ_s and μ_s, as

$$\kappa_s = \lambda_s + \frac{2}{3}\mu_s, \tag{10}$$

$\boldsymbol{I}$ is the second-order identity tensor and $\mathbf{I}'$ is a fouth-order tensor computed as

$$\mathbf{I}' = \mathbf{I} - \frac{1}{3}\boldsymbol{I} \otimes \boldsymbol{I} \tag{11}$$

where $\mathbf{I}$ is the fouth-order symmetric identity tensor computed as $\mathrm{I}_{ijkl} = \frac{1}{2}\left(\delta_{ik}\delta_{jl} + \delta_{il}\delta_{kj}\right)$.

The material time derivative of the Cauchy stress rate is computed from the Jaumann measure of the Cauchy stress rate tensor as

$$\dot{\boldsymbol{\sigma}} = \boldsymbol{\sigma}^{\triangledown J} + \boldsymbol{\Omega} \tag{12}$$

where $\boldsymbol{\Omega}$ is a tensor that accounts for the rotations defined as

$$\boldsymbol{\Omega} = \boldsymbol{W} \cdot \boldsymbol{\sigma} + \boldsymbol{\sigma} \cdot \boldsymbol{W}^T \tag{13}$$

where $\boldsymbol{W}$ is the spin tensor

$$W_{ij} = \frac{1}{2}\left(\frac{\partial v_i}{\partial x_j} - \frac{\partial v_j}{\partial x_i} \right) \tag{14}$$

In this work, tensor $\boldsymbol{\Omega}$ is computed at the end of each time step.

Discretizing in time Eq.(12) for the time step interval $[{}^n t, {}^{n+1} t]$ and expanding the Cauchy stress rate, yields

$$\frac{{}^{n+1}\boldsymbol{\sigma} - {}^{n}\boldsymbol{\sigma}}{\Delta t} = \boldsymbol{c}^{\sigma J} : {}^{n+1}\boldsymbol{d} + {}^{n}\boldsymbol{\Omega} \tag{15}$$

In Eq.(15), $\boldsymbol{\Omega}$ can be viewed as a correction of the Cauchy stress tensor. So it can be added to the Cauchy stress tensor of the previous time step as follows

$$^{n}\hat{\boldsymbol{\sigma}} = {}^{n}\boldsymbol{\sigma} + {}^{n}\boldsymbol{\Omega} \tag{16}$$

Replacing Eq.(16) in (15), yields

$$\frac{^{n+1}\boldsymbol{\sigma} - {}^{n}\hat{\boldsymbol{\sigma}}}{\Delta t} = \boldsymbol{c}^{\sigma J} : {}^{n+1}\boldsymbol{d} \tag{17}$$

Substituting in Eq.(18) the relation for $\boldsymbol{c}^{\sigma J}$ using Eq.(9), yields

$$\frac{^{n+1}\boldsymbol{\sigma} - {}^{n}\hat{\boldsymbol{\sigma}}}{\Delta t} = (\kappa_s \boldsymbol{I} \otimes \boldsymbol{I} + 2\mu_s \mathbf{I}') : {}^{n+1}\boldsymbol{d} \tag{18}$$

Hence,

$$\frac{^{n+1}\boldsymbol{\sigma} - {}^{n}\hat{\boldsymbol{\sigma}}}{\Delta t} = \underbrace{\kappa_s \left(\boldsymbol{I} \otimes \boldsymbol{I}\right) : {}^{n+1}\boldsymbol{d}}_{^{n+1}\dot{p}} + \underbrace{2\mu_s \mathbf{I}' : {}^{n+1}\boldsymbol{d}}_{^{n+1}\dot{\boldsymbol{\sigma}}'} \tag{19}$$

The first and the second terms of the right hand side of Eq.(20) represent the increments in time of the volumetric and deviatoric parts of the Cauchy stress tensor.

From Eq.(20) one may compute the updated stresses using the velocities only or both the pressure and the velocities, as follows

$$^{n+1}\boldsymbol{\sigma} = {}^{n}\hat{\boldsymbol{\sigma}} + \Delta t \left(\kappa_s \boldsymbol{I} \otimes \boldsymbol{I} + 2\mu_s \mathbf{I}'\right) : {}^{n+1}\boldsymbol{d} \tag{20}$$

$$^{n+1}\boldsymbol{\sigma} = {}^{n}\hat{\boldsymbol{\sigma}} + {}^{n+1}\Delta p \boldsymbol{I} + 2\Delta t \mu_s \mathbf{I}' : {}^{n+1}\boldsymbol{d} \tag{21}$$

Eqs.(21) and (23) will be used for computing the Cauchy stress tensor in the Velocity (V) and mixed Velocity-Pressure (VP) formulations, respectively.

3.2. Quasi-incompressible Newtonian fluids

The standard form of the constitutive relation for a Newtonian fluid reads

$$\boldsymbol{\sigma} = \boldsymbol{\sigma'} + p\boldsymbol{I} = 2\mu_f \boldsymbol{d}' + p\boldsymbol{I} \tag{22}$$

where μ_f is the fluid viscosity.

Quasi-incompressible fluids have a compressibility that is small enough to neglect the variations of density on time. However, unlike fully incompressible

materials, they are not totally divergence-free and the volumetric strain rate is related to the variation in time of pressure via Eq.(4). Considering a time interval $[n, n+1]$ for quasi-incompressible Newtonian fluids the following relation holds

$$^{n+1}p = {}^{n}p + \Delta t \kappa_f {}^{n+1}d^v \tag{23}$$

Subsituting Eq.(27) into (25) yields

$$^{n+1}\boldsymbol{\sigma} = (2\mu_f \mathbf{I}' + \Delta t \kappa_f \boldsymbol{I} \otimes \boldsymbol{I}) : \boldsymbol{d} + {}^{n}p\boldsymbol{I} \tag{24}$$

where $\mathbf{I}'$ is the fourth-order tensor defined in Eq.(11).

For convenience, Eq.(29) is rewritten as

$$^{n+1}\Delta\boldsymbol{\sigma} = {}^{n+1}\boldsymbol{\sigma} - {}^{n}\boldsymbol{\sigma} = \boldsymbol{c}^{\sigma}_{NF} : \boldsymbol{d} \tag{25}$$

where the following substitutions have been done:

$$^{n}\boldsymbol{\sigma} = {}^{n}p\boldsymbol{I} \tag{26}$$

$$\boldsymbol{c}^{\sigma}_{NF} = 2\mu_f \mathbf{I}' + \Delta t \kappa_f \boldsymbol{I} \otimes \boldsymbol{I} \tag{27}$$

The aim of the Unified formulation is to reduce the differences in the analysis of fluids and solids. For this reason, the quasi-incompressible Newtonian constitutive law is written for the stress rate, similarly as for the hypoelastic model for solids. For Newtonian fluids, the rate of Cauchy stress can be simply computed with the material time derivative. Hence

$$\boldsymbol{\sigma}^{\triangledown} = \dot{\boldsymbol{\sigma}} = \frac{\Delta\boldsymbol{\sigma}}{\Delta t} = \frac{\boldsymbol{c}^{\sigma}_{NF}}{\Delta t} : \boldsymbol{d} = \boldsymbol{c}^{\triangledown\sigma}_{NF} : \boldsymbol{d} \tag{28}$$

where the tangent moduli tensor for the rate of the Cauchy stress $\boldsymbol{c}^{\triangledown\sigma}_{NF}$ is

$$\boldsymbol{c}^{\triangledown\sigma}_{NF} = \frac{2\mu_f}{\Delta t}\mathbf{I}' + \kappa_f \boldsymbol{I} \otimes \boldsymbol{I} \tag{29}$$

Note that Eq.(33) has the same structure as Eq.(7).

For a 2D problem, $\boldsymbol{c}^{\triangledown\sigma}_{NF} = \begin{bmatrix} \kappa_f + \frac{4}{3\Delta t}\mu_f & \kappa_f - \frac{2}{3\Delta t}\mu_f & 0 \\ \kappa_f - \frac{2}{3\Delta t}\mu_f & \kappa_f + \frac{4}{3\Delta t}\mu_f & 0 \\ 0 & 0 & \frac{\mu_f}{\Delta t} \end{bmatrix}$

4. Linearization of the momentum equations

In the UL description used in this work, the governing equations are integrated over the unknown configuration Ω (the so-called updated configuration) and the space derivatives are computed with respect to the spatial coordinates.

From Eq.(1), integrating over Ω and after standard transformations, the Galerkin approximation of the Principle of Virtual Power for a node I is obtained as [30]

$$\underbrace{\int_\Omega N_I \rho d\Omega \ \dot{v}_i}_{f_{Ii}^{dyn}} + \underbrace{\int_\Omega \frac{\partial N_I}{\partial x_j}\sigma_{ij} d\Omega}_{f_{Ii}^{int}} = \underbrace{\int_\Omega N_I b_i d\Omega + \int_{\Gamma_t} N_I t_i^p d\Gamma}_{f_{Ii}^{ext}} \tag{30}$$

where N_I is the linear shape function for node I and $\boldsymbol{f}^{dyn}$, $\boldsymbol{f}^{int}$ and $\boldsymbol{f}^{ext}$ are the dynamic, internal and external force vectors, respectively, expressed in the UL framework.

For convenience, the linearization of the internal forces $\boldsymbol{f}^{int}$ is performed in the known configuration Ω_0, as for a total Lagrangian (TL) description. The UL linearized form will be obtained by push-forward transformations on the TL form. Instead, the linearization of the dynamics forces $\boldsymbol{f}^{dyn}$ will be performed directly in the updated configuration.

4.1. Internal components of the tangent matrix

Applying a standard pull back tranformation to $\boldsymbol{f}^{int}$ from the unknown domain Ω to the known one Ω_0 [30], the internal forces for a TL description ${}^{TL}\boldsymbol{f}^{int}$ read

$${}^{TL}f_{Ii}^{int} = \int_{\Omega_0} \frac{\partial N_I}{\partial X_j} P_{ij} d\Omega_0 \tag{31}$$

where $\boldsymbol{P}$ is the first Piola-Kirchhoff stress tensor. All the variables with vectors subscript $(\cdot)_0$ refer to the last known configuration. For the sake of clarity, the terms referred to the TL description are denoted with the left upper index ${}^{TL}(\cdot)$. Unless otherwise specified, the variables belong to the UL description.

In the proposed Unified formulation, the constitutive relations for both fluids and solids are expressed in rate form. Hence it is more convenient to perform the

linearization of the material derivative of the internal forces and then integrate for the time step increment Δt. The material time derivative of Eq.(36) is

$$^{TL}\dot{f}_{Ii}^{int} = \int_{\Omega_0} \frac{\partial N_I}{\partial X_j} \dot{P}_{ij} d\Omega_0 \tag{32}$$

The first Piola-Kirchhoff stress tensor $\boldsymbol{P}$ is not typically used because it is not symmetric and its rate is a non-objective measure. For these reasons, in the TL framework it is more convenient to work with the second Piola-Kirchhoff stress tensor $\boldsymbol{S}$ and its rate. These stress rate measures are related each other via the following relation

$$\dot{P}_{ij} = \dot{S}_{ir} F_{rj}^T + S_{ir} \dot{F}_{rj}^T \tag{33}$$

where $\boldsymbol{F}$ is the deformation gradient tensor defined as

$$F_{ij} = \frac{\partial x_i}{\partial X_j} \tag{34}$$

Substituting Eq.(38) into (37), and analyzing an infinitesimal increment yields

$$^{TL}\delta\dot{f}_{Ii}^{int} = \underbrace{\int_{\Omega_0} \frac{\partial N_I}{\partial X_j} F_{ir} \delta\dot{S}_{jr} d\Omega_0}_{^{TL}\delta\dot{f}_{Ii}^{m}} + \underbrace{\int_{\Omega_0} \frac{\partial N_I}{\partial X_j} S_{ir} \delta\dot{F}_{rj}^T d\Omega_0}_{^{TL}\delta\dot{f}_{Ii}^{g}} \tag{35}$$

In Eq.(40) the increment of the material time derivative of the internal forces has been split into the material and the geometric parts, $^{TL}\delta\dot{\boldsymbol{f}}^m$ and $^{TL}\delta\dot{\boldsymbol{f}}^g$, respectively. The former accounts for the material response through the rate of the second Piola-Kirchhoff stress tensor. The second term is the initial stress term that contains the information of the updated stress field.

4.1.1. Material tangent matrix

The rate of the second Piola-Kirchhoff stress tensor $\boldsymbol{S}$ is related to the deformation rate through the tangent constitutive tensor as

$$\dot{S}_{ij} = C_{ijkl} \dot{E}_{kl} \tag{36}$$

where $\boldsymbol{C}$ is a fourth-order tensor and $\boldsymbol{E}$ is the Green-Lagrange strain tensor.

Substituting Eq.(41) into the term $^{TL}\delta\dot{\boldsymbol{f}}^m$ of Eq.(40), yields

$$^{TL}\delta\dot{f}_{Ii}^{m} = \int_{\Omega_0} \frac{\partial N_I}{\partial X_j} F_{ir} C_{jrkl} \delta\dot{E}_{kl} d\Omega_0 \tag{37}$$

The Green-Lagrange strain tensor can be expressed in terms of the nodal velocities as

$$\dot{E}_{kl} = \frac{\partial N_J}{\partial X_s} F_{kl} \bar{v}_{sJ} \tag{38}$$

In Eq.(43) and in the following, $\bar{(\cdot)}$ denotes a nodal value (*e.g.* $\bar{v}_{sJ}$ is the s-component of the velocity of node J).

Substituting Eq.(43) in (42), yields

$${}^{TL}\delta \dot{f}^m_{Ii} = \int_{\Omega_0} \frac{\partial N_I}{\partial X_j} F_{rj} C_{ijkl} \frac{\partial N_J}{\partial X_s} F_{kl} d\Omega_0 \ \delta \bar{v}_{sJ} \tag{39}$$

In order to obtain the increment of the internal forces, the material time derivative of the internal forces increment is integrated over a time step increment Δt as

$${}^{TL}\delta \boldsymbol{f}^m = {}^{TL}\delta \dot{\boldsymbol{f}}^m \Delta t \tag{40}$$

From Eqs.(44) and (45), yields

$${}^{TL}\delta f^m_{Ii} = \int_{\Omega_0} \frac{\partial N_I}{\partial X_j} F_{rj} \Delta t C_{ijkl} \frac{\partial N_J}{\partial X_s} F_{kl} d\Omega_0 \ \delta \bar{v}_{Js} \tag{41}$$

The material tangent matrix for the UL framework is obtained by applying a push-forward transformation on each term of Eq.(46) and integrating over the updated domain Ω. The following relations hold

$$d\Omega_0 = \frac{d\Omega}{J} \tag{42}$$

$$\frac{\partial N_I}{\partial X_j} = \frac{\partial N_I}{\partial x_k} F_{kj} \tag{43}$$

$$C^{\nabla\sigma}_{ijkl} = F^{-1}_{mi} F^{-1}_{nj} F^{-1}_{ok} F^{-1}_{pl} c^{\nabla\sigma}_{mnop} J \tag{44}$$

where $c^{\nabla\sigma}$ is the tangent moduli for the rate of the Cauchy stress $\boldsymbol{\sigma}^{\nabla}$.

Substituting Eqs.(47-49) into (46) and using the minor symmetries, yields

$$\delta f^m_{Ir} = \int_{\Omega} \frac{\partial N_I}{\partial x_k} \delta_{ri} \Delta t \ c^{\nabla\sigma}_{kijl} \frac{\partial N_J}{\partial x_l} \delta_{sj} d\Omega \ \delta \bar{v}_{Js} \tag{45}$$

Therefore, the expressions of the material tangent matrix for the velocity increments in UL framework in the indicial and Voigt notation read, respectively

$$K^m_{IJrs} = \int_{\Omega} \frac{\partial N_I}{\partial x_k} \delta_{ri} \Delta t \ c^{\nabla\sigma}_{kijl} \frac{\partial N_J}{\partial x_l} \delta_{sj} d\Omega \ , \ \boldsymbol{K}^m_{IJ} = \int_{\Omega^e} \boldsymbol{B}^T_I \Delta t \left[\boldsymbol{c}^{\nabla\sigma}\right] \boldsymbol{B}_J d\Omega \tag{46}$$

For the node I of a 2D element, matrix $\boldsymbol{B}$ is

$$\mathbf{B}_I = \begin{bmatrix} \dfrac{\partial N_I}{\partial x} & 0 & \dfrac{\partial N_I}{\partial y} \\ 0 & \dfrac{\partial N_I}{\partial y} & \dfrac{\partial N_I}{\partial x} \end{bmatrix}^T \tag{47}$$

4.1.2. Geometric tangent matrix

The geometric tangent matrix in the UL framework is derived using the same procedure as for the material component.

From Eq.(40)

$$^{TL}\delta \dot{f}^g_{Ii} = \int_{\Omega_0} \frac{\partial N_I}{\partial X_j} S_{ir} \delta \dot{F}^T_{rj} d\Omega_0 \tag{48}$$

where the rate of the deformation gradient $\dot{\boldsymbol{F}}$ is defined as

$$\dot{F}_{ij} = \frac{\partial N_J}{\partial X_i} \bar{v}_{Jj} \tag{49}$$

Substituting Eq.(54) into Eq.(53), the geometric components of the internal power in the TL description can be written as

$$^{TL}\delta \dot{f}^g_{Ii} = \int_{\Omega_0} \frac{\partial N_I}{\partial X_j} S_{ir} \frac{\partial N_J}{\partial X_r} d\Omega_0 \ \delta \bar{v}_{Jj} \tag{50}$$

Integrating Eq.(55) in time for a time step increment Δt yields

$$^{TL}\delta f^g_{Ii} = \int_{\Omega_0} \frac{\partial N_I}{\partial X_j} \Delta t S_{ir} \frac{\partial N_J}{\partial X_r} d\Omega \ \delta \bar{v}_{Jj} \tag{51}$$

In order to recover the UL form, the Piola identity has to be recalled, *i.e.*

$$\boldsymbol{S} = \boldsymbol{F}^{-1} \boldsymbol{\sigma} \boldsymbol{F}^{-T} J \tag{52}$$

Substituting Eqs.(47), (48) and (57) into (56) and using the symmetries, yields

$$\delta f^g_{Ir} = \int_{\Omega} \frac{\partial N_I}{\partial x_j} \Delta t \sigma_{jk} \frac{\partial N_J}{\partial x_k} d\Omega \delta_{rs} \delta \bar{v}_{Js} \tag{53}$$

The geometric part of the tangent matrix for the increments of velocity is obtained from Eq.(58) as

$$K^g_{IJrs} = \int_{\Omega} \frac{\partial N_I}{\partial x_j} \Delta t \sigma_{jk} \frac{\partial N_J}{\partial x_k} d\Omega \delta_{rs} \ , \ \boldsymbol{K}^g_{IJ} = \boldsymbol{I} \int_{\Omega} \boldsymbol{\beta}^T_I \Delta t \boldsymbol{\sigma} \boldsymbol{\beta}_J d\Omega \tag{54}$$

where for 2D problems $\boldsymbol{\beta}_I = \begin{bmatrix} \dfrac{\partial N_I}{\partial x} & \dfrac{\partial N_I}{\partial y} \end{bmatrix}^T$.

4.2. Dynamic component of the tangent matrix

In this work, the implicit Newmark's integration rule has been adopted. In particular, the Newmark's parameters chosen are $\beta = \frac{1}{4}$ and $\gamma = \frac{1}{2}$ [30]. According to this unconditionally stable scheme, the accelerations $\dot{\mathbf{v}}$ and the displacements $\boldsymbol{u}$ are computed, respectively, as

$$^{n+1}\dot{\mathbf{v}} = \frac{2}{\Delta t}\left(^{n+1}\boldsymbol{v} - {}^{n}\boldsymbol{v}\right) - {}^{n}\dot{\mathbf{v}} \tag{55}$$

$$^{n+1}\boldsymbol{u} = {}^{n}\boldsymbol{u} + \frac{\Delta t}{2}\left(^{n+1}\boldsymbol{v} + {}^{n}\boldsymbol{v}\right) \tag{56}$$

Replacing Eq.(60) into the dynamic term f_{Ii}^{dyn} of Eq.(35), and differentiating with respect to velocity increments, the dynamic component of the tangent matrix (also known as the mass matrix) is obtained as

$$K_{IJij}^{\rho} = \delta_{ij}\int_{\Omega} N_I \frac{2\rho}{\Delta t} N_J d\Omega \ , \ \boldsymbol{K}_{IJ}^{\rho} = \boldsymbol{I}\int_{\Omega} N_I \frac{2\rho}{\Delta t} N_J d\Omega \tag{57}$$

4.3. Incremental solution scheme

The linear momentum equations are solved iteratively for the velocity increments. For each iteration i the following linear system is solved

$$\boldsymbol{K}^i \boldsymbol{\Delta}\bar{\boldsymbol{v}} = \boldsymbol{R}^i \tag{58}$$

with

$$\boldsymbol{K}^i = \boldsymbol{K}^m(^{n+1}\bar{\boldsymbol{x}}^i, \boldsymbol{c}^{\nabla\sigma}) + \boldsymbol{K}^g(^{n+1}\bar{\boldsymbol{x}}^i, \boldsymbol{\sigma}^i) + \boldsymbol{K}^{\rho}(^{n+1}\bar{\boldsymbol{x}}^i) \tag{59}$$

where $\boldsymbol{K}_{IJ}^{m}$, $\boldsymbol{K}_{IJ}^{g}$ and $\boldsymbol{K}_{IJ}^{\rho}$ are respectively given in Eq.(51), Eq.(59) and Eq.(62), and

$$R_{Ii}^i = \int_{\Omega} N_I \rho N_J d\Omega \ \bar{v}_{Ji}^i + \int_{\Omega} \frac{\partial N_I}{\partial x_j}\sigma_{ij}^i d\Omega - \int_{\Omega} N_I {}^{n+1}b_i d\Omega - \int_{\Gamma_t} N_I {}^{n+1}t_i^p d\Gamma \tag{60}$$

The fourth-order constitutive tangent moduli tensor $\boldsymbol{c}^{\nabla\sigma}$ of matrix $\boldsymbol{K}^m$ (Eq.(51)) is $\boldsymbol{c}_{NF}^{\nabla\sigma}$ (Eq.(34)) for a Newtonian fluid while for a hypoelastic solid is $\boldsymbol{c}^{\sigma J}$ (Eq.(9)).

In the analysis of quasi-incompressible Newtonian fluids, the volumetric part of the material component of the tangent matrix $\boldsymbol{K}^m$ can compromise the conditioning of the linear system [31, 32, 33]. In order to prevent the numerical

instabilities originated by the ill-conditioning of the tangent matrix, the actual bulk modulus of the fluid κ_f is substituted by a reduced pseudo bulk modulus κ_p, defined as a $\kappa_p = \theta\kappa_f$. The pseudo bulk modulus is predicted *a priori* using the strategy described in [34].

For Newtonian fluids the stress tensor $\boldsymbol{\sigma}$ is computed with Eq.(29). For hypoelastic solids, if a velocity formulation is used the stresses are computed via Eq.(21). In the context of a mixed velocity-pressure formulation, the Cauchy stress tensor $\boldsymbol{\sigma}$ is computed with Eq.(23).

5. Discretized form of the mass balance equation

For the VP-element the continuity equation is solved in the standard non-stabilized form of Eq.(4). The Galerkin approximation of Eq.(4) for the same linear shape functions $\boldsymbol{N}$ used for the velocity is

$$\int_\Omega N_I \frac{1}{\kappa_s} N_J D\dot{p_J} d\Omega - \int_\Omega N_I \frac{\partial N_J}{\partial x_i} \bar{v}_{iJ} d\Omega = 0 \tag{61}$$

Regarding the time integration, a first order scheme has been adopted for the pressure. Hence, for a time interval $[{}^n t, {}^{n+1} t]$ of duration Δt the first and the second variations in time of the pressure are computed as

$${}^{n+1}\dot{\mathbf{p}} = \frac{{}^{n+1}\mathbf{p} - {}^{n}\mathbf{p}}{\Delta t} \tag{62}$$

$${}^{n+1}\ddot{\mathbf{p}} = \frac{{}^{n+1}\mathbf{p} - {}^{n}\mathbf{p}}{\Delta t^2} - \frac{{}^{n}\dot{\mathbf{p}}}{\Delta t} \tag{63}$$

Introducing Eq.(67) in (66), the discretized form of the continuity equation solved for the pressure is

$$\frac{1}{\Delta t} \boldsymbol{M}_1 {}^{n+1}\bar{\boldsymbol{p}} = \frac{1}{\Delta t} \boldsymbol{M}_1 {}^{n}\bar{\boldsymbol{p}} + \boldsymbol{Q}^{T\,n+1}\bar{\boldsymbol{v}} \tag{64}$$

where the matrices introduced in Eq.(69) are defined in Box 1.

6. Stabilized FIC form of the mass balance equation

In order to deal with quasi and fully incompressible materials the numerical scheme needs to be stabilized. This is because the interpolation orders of the

$$M_{1_{IJ}} = \int_{\Omega^e} N_I \frac{1}{\kappa_s} N_J d\Omega \ , \ \mathbf{Q}_{IJ} = \int_{\Omega^e} \mathbf{B}_I^T \mathbf{m} N_J d\Omega \ \text{ with } \ \mathbf{m} = [1,1,0]^T$$

Box 1. Matrices and vectors of the continuity equation (Eq.(69)) for the VP-element.

velocity and pressure fields do not fullfil the so-called *LBB inf − sup condition* [2]. The required stabilization is introduced for both the VPS/F and the VPS/S elements via the Finite Calculus (FIC) technique presented in [1]. In the mentioned work, a FIC stabilized finite element formulation for quasi-incompressible Newtonian fluids is derived and validated for several free surface flow problems, highlighting its excellent mass preservation features. The derivation of the stabilization technique lies outside the objectives of this work and the details can be found in [1]. Basically, the linear momentum equations do not change and are counted, with both the second order FIC form in space and the first order FIC form in time of the quasi-incompressible mass balance equation [7, 8], for deriving the stabilized form of the mass balance equation in a consistent manner.

For the VPS/F-element the same FIC form of the mass balance equation derived in [1] can be used because both refer to Newtonian fluids. Hence, for the VPS/F-element, the FIC-stabilized form of the mass balance equation, after FEM discretization, reads

$$\int_\Omega \frac{1}{\kappa_f} \mathbf{N}^T \mathbf{N} \frac{D\bar{\mathbf{p}}}{Dt} d\Omega + \int_\Omega \frac{\tau_f \rho}{\kappa_f} \mathbf{N}^T \mathbf{N} \frac{D^2\bar{\mathbf{p}}}{Dt^2} d\Omega - \int_\Omega \mathbf{N}^T \mathbf{m}^T \mathbf{B} \bar{\mathbf{v}} d\Omega + \\ + \int_\Omega \tau_f (\boldsymbol{\nabla}\mathbf{N})^T \boldsymbol{\nabla}\mathbf{N} \bar{\mathbf{p}} d\Omega + \int_{\Gamma_t} \frac{2\tau_f}{h_n} \mathbf{N}^T \mathbf{N} \bar{\mathbf{p}} d\Gamma - \mathbf{f}_p = 0 \tag{65}$$

where for triangular elements

$$\boldsymbol{\nabla}\mathbf{N}^T = \begin{bmatrix} \boldsymbol{\nabla} N_1 \\ \boldsymbol{\nabla} N_2 \\ \boldsymbol{\nabla} N_3 \end{bmatrix} \text{ with } \boldsymbol{\nabla} = \begin{Bmatrix} \dfrac{\partial}{\partial x} \\ \dfrac{\partial}{\partial y} \end{Bmatrix} \text{ and } \ \mathbf{N} = [\mathbf{N}_1, \mathbf{N}_2, \mathbf{N}_3]^T \tag{66}$$

and τ is the stabilization parameter given by

$$\tau_f = \left(\frac{8\mu_f}{h^2} + \frac{2\rho}{\delta} \right)^{-1} \tag{67}$$

where h and δ are characteristic distances in space and time, respectively. In practice, h and δ have the same order of magnitude of the element size and the time step increment, respectively. Details of the derivation of Eq.(70) can be found in [1].

In order to use the same form of Eq.(70) [1] for quasi-incompressible hypoelastic solids as for the VPS/F-element, the fluid parameters (the viscosity μ_f and the bulk modulus κ_f) are substituted by the equivalent parameters for the solid. The similarity between the constitutive expression for Newtonian fluids and hypoelastic solids is evident comparing the computation of the Cauchy stress tensor increment for both cases.

For quasi-incompressible Newtonian fluids Eq.(30) holds and, for clarity purposes, here is rewritten as

$$^{n+1}\Delta\boldsymbol{\sigma}_f = 2\mu_f \mathbf{I}' : \boldsymbol{d} - \Delta t \kappa_f \boldsymbol{I} \otimes \boldsymbol{I} : \boldsymbol{d} \tag{68}$$

From Eqs.(20), the increment of the Cauchy stress for hypoelastic solids is

$$^{n+1}\Delta\boldsymbol{\sigma}_s = 2\Delta t \mu_s \mathbf{I}' : \boldsymbol{d} - \Delta t \kappa_s \boldsymbol{I} \otimes \boldsymbol{I} : \boldsymbol{d} \tag{69}$$

where κ_s is the bulk modulus for the solid and μ_s is the second Lamè parameter.

Eqs.(73) and (74) show the duality between hypoelastic and Newtonian quasi-incompressible constitutive laws. In the latter the deviatoric and the volumetric parts of the Cauchy stress tensor are controled by the dynamic viscosity μ_f and the bulk modulus κ_f, respectively. The equivalent roles in hypoelastic solids are taken by the second Lamè parameter scaled by the time increment ($\Delta t \mu_s$) and the bulk modulus κ_s.

Thanks to this equivalence, the FIC-based stabilized mass continuity equation for the VPS/S hypoelastic element can be written (after FEM discretization) as

$$\int_\Omega \frac{1}{\kappa_s} \mathbf{N}^T \mathbf{N} \frac{D\bar{\mathbf{p}}}{Dt} d\Omega + \int_\Omega \frac{\tau_s \rho}{\kappa_s} \mathbf{N}^T \mathbf{N} \frac{D^2\bar{\mathbf{p}}}{Dt^2} d\Omega - \int_\Omega \mathbf{N}^T \mathbf{m}^T \mathbf{B} \bar{\mathbf{v}} d\Omega + \\ + \int_\Omega \tau_s (\boldsymbol{\nabla}\mathbf{N})^T \boldsymbol{\nabla}\mathbf{N} \bar{\mathbf{p}} d\Omega + \int_{\Gamma_t} \frac{2\tau_s}{h_n} \mathbf{N}^T \mathbf{N} \bar{\mathbf{p}} d\Gamma - \mathbf{f}_p = 0 \tag{70}$$

where τ_s is the stabilization parameter given by

$$\tau_s = \left(\frac{8\Delta t \mu_s}{h^2} + \frac{2\rho}{\delta} \right)^{-1} \tag{71}$$

We highlight again the analogy between the discretized (stabilized) FIC-form of the mass balance equation for fluids (Eq.(70)) and solids (Eq.75).

Eqs.(70) and (75) can be written in an unified matrix form for both fluids and solids as

$$\mathbf{M}_{1(f,s)}\dot{\bar{\mathbf{p}}} + \mathbf{M}_{2(f,s)}\ddot{\bar{\mathbf{p}}} - \mathbf{Q}^T\bar{\mathbf{v}} + (\mathbf{L}_{(f,s)} + \mathbf{M}_{b(f,s)})\bar{\mathbf{p}} - \mathbf{f}_{p(f,s)} = \mathbf{0} \tag{72}$$

The matrices and vectors in Eq.(77) for Newtonian fluids (VPS/F-element) and hypoelastic solids (VPS/S-element) are given in Box 2 and 3, respectively.

$$M_{1f_{IJ}} = \int_\Omega \frac{1}{\kappa_f} N_I N_J d\Omega \ , \ M_{2f_{IJ}} = \int_\Omega \tau_f \frac{\rho}{\kappa_f} N_I N_J d\Omega$$
$$M_{bf_{IJ}} = \int_{\Gamma_t} \frac{2\tau_f}{h_n} N_I N_J d\Gamma \ , \ L_{f_{IJ}} = \int_\Omega \tau_f (\boldsymbol{\nabla}^T N_I) \boldsymbol{\nabla} N_J d\Omega$$
$$f_{pf_I} = \int_{\Gamma_t} \tau_f N_I \left[\rho \frac{Dv_n}{Dt} - \frac{2}{h_n}(2\mu_f d_n - t_n) \right] d\Gamma - \int_{\Omega^e} \tau_f \boldsymbol{\nabla}^T N_I \mathbf{b} d\Omega$$

Box 2. Matrices and vectors of Eq.(77) for the VPS/F-element.

$$M_{1s_{IJ}} = \int_\Omega \frac{1}{\kappa_s} N_I N_J d\Omega \ , \ M_{2s_{IJ}} = \int_\Omega \tau_s \frac{\rho}{\kappa_s} N_I N_J d\Omega$$
$$M_{bs_{IJ}} = \int_{\Gamma_t} \frac{2\tau_s}{h_n} N_I N_J d\Gamma \ , \ L_{s_{IJ}} = \int_\Omega \tau_s (\boldsymbol{\nabla}^T N_I) \boldsymbol{\nabla} N_J d\Omega$$
$$f_{ps_I} = \int_{\Gamma_t} \tau_s N_I \left[\rho \frac{Dv_n}{Dt} - \frac{2}{h_n}(2\Delta t \mu_s d_n - t_n) \right] d\Gamma - \int_{\Omega^e} \tau_s \boldsymbol{\nabla}^T N_I \mathbf{b} d\Omega$$

Box 3. Matrices and vectors of Eq.(77) for the VPS/S-element.

Introducing the time integration of the pressure (Eqs.(67) and (68)) into Eq.(77) and solving the stabilized continuity equation for the nodal pressures, yields

$$\boldsymbol{H}_{f,s}\bar{\boldsymbol{p}}^{i+1} = \boldsymbol{F}_{p(f,s)}(\bar{\boldsymbol{v}}, \bar{\boldsymbol{p}}) \tag{73}$$

where

$$\boldsymbol{H}_{f,s} = \left(\frac{1}{\Delta t} \mathbf{M}_{1(f,s)} + \frac{1}{\Delta t^2} \mathbf{M}_{2(f,s)} + \mathbf{L}_{f,s} + \mathbf{M}_{b(f,s)} \right) \tag{74}$$

and

$$\boldsymbol{F}_{p(f,s)} = \frac{\mathbf{M}_{1(f,s)}}{\Delta t} {}^{n}\bar{\boldsymbol{p}} + \frac{\mathbf{M}_{2(f,s)}}{\Delta t^2} \left({}^{n}\bar{\boldsymbol{p}} + {}^{n}\dot{\bar{\boldsymbol{p}}} \Delta t \right) + \mathbf{Q}^T \, \bar{\mathbf{v}} + \mathbf{f}_{p(f,s)} \tag{75}$$

7. Solution scheme

Each time step is solved using a two-step Gauss-Seidel iterative procedure. First the linear momentum equations are solved for the velocity increments according to Eq.(63). Then the continuity equation is solved for the pressure in the updated configuration. For the VPS/F-element the stabilized form of Eq.(78) is solved using the matrices of Box 1. For quasi-incompressible solids, the VPS/S-element is used, hence the continuity equation is solved using the stabilized form of Eq.(78) and the matrices given in Box 2. Instead, for solids far from the incompressible limit, both the V and the VP elements can be used. With the VP-element, the non-stabilized form of the continuity equation (Eq.(69)) is solved. On the contrary, if the V-element is used the continuity equation is not computed. In Table **??**, the essential feature of each one of the elements presented in this work are summarized.

	Element			
	V	**VP**	**VPS/S**	**VPS/F**
Constitutive law	Hypoelastic solid	Hypoelastic solid	Hypoelastic solid	Newtonian fluid
Momentum equations	Eq.(63)	Eq.(63)	Eq.(63)	Eq.(63)
$\boldsymbol{c}^{\nabla\sigma}$	$\boldsymbol{c}^{\sigma J}$, Eq.(9)	$\boldsymbol{c}^{\sigma J}$, Eq.(9)	$\boldsymbol{c}^{\sigma J}$, Eq.(9)	$\boldsymbol{c}^{\nabla\sigma}_{NF}$, Eq.(34)
$\boldsymbol{\sigma}$	Eq.(21)	Eq.(23)	Eq.(23)	Eq.(29)
Continuity equation	-	Eq.(69) Box 1	Eq.(78) Box 3	Eq.(78) Box 2

Table 1: Essential features of the V, VP, VPS/S and VPS/F elements.

Concerning the degrees of freedom, each node of the mesh is characterized by a single set of kinematic variables. This means that the degrees of freedom for the solid and fluid velocities coincide also at the interface nodes. In order to guarantee the correct boundary conditions for the stresses, each interface node has a degree of freedom for the pressure of the fluid and for the pressure of the solid. This requires solving twice the continuity equation: once for the VPS/F-element and once for the VP or the VPS/S solid elements.

For the sake of clarity, the coupling algorithms for the V-element and the mixed elements (the VP and VPS/S elements) are presented separately.

For a generic time interval $[{}^{n}t, {}^{n+1}t]$, Algorithm 7 describes all the steps required for solving the FSI problem using for fluids the VPS/F-element and for solids the V-element.

For each iteration i:

1. Compute the nodal velocity increments $\boldsymbol{\Delta\bar{v}}_{s,f}$:

$\boldsymbol{K}^i_{s,f}\boldsymbol{\Delta\bar{v}}_{s,f} = \boldsymbol{R}^i_{s,f}(\bar{\boldsymbol{v}}^i_{s,f}, \bar{\boldsymbol{p}}^i_f)$

where for fluids $\boldsymbol{K}^i_f = \boldsymbol{K}^m(\bar{\boldsymbol{x}}^i, \boldsymbol{c}^{\triangledown\sigma}_{NF}) + \boldsymbol{K}^g(\bar{\boldsymbol{x}}^i, \boldsymbol{\sigma}^i_f) + \boldsymbol{K}^\rho(\bar{\boldsymbol{x}}^i)$

and for solids $\boldsymbol{K}^i_s = \boldsymbol{K}^m(\bar{\boldsymbol{x}}^i, \boldsymbol{c}^{\sigma J}) + \boldsymbol{K}^g(\bar{\boldsymbol{x}}^i, \boldsymbol{\sigma}^i_s) + \boldsymbol{K}^\rho(\bar{\boldsymbol{x}}^i)$

2. Update the nodal velocities: ${}^{n+1}\bar{\boldsymbol{v}}^{i+1}_{s,f} = {}^{n+1}\bar{\boldsymbol{v}}^i_{s,f} + \boldsymbol{\Delta\bar{v}}_{s,f}$

3. Update the nodal coordinates: ${}^{n+1}\bar{\boldsymbol{x}}^{i+1}_{s,f} = {}^{n+1}\bar{\boldsymbol{x}}^i_{s,f} + \bar{\boldsymbol{u}}_{s,f}(\boldsymbol{\Delta\bar{v}}_{s,f})$

4. Compute the fluid nodal pressures $\bar{\boldsymbol{p}}^{i+1}_f$: $\boldsymbol{H}_f\bar{\boldsymbol{p}}^{i+1}_f = \boldsymbol{F}_{pf}(\bar{\boldsymbol{v}}^{i+1}_f, \bar{\boldsymbol{p}}^i_f)$

where $\boldsymbol{H}_f = \left(\frac{1}{\Delta t}\mathbf{M}_{1f} + \frac{1}{\Delta t^2}\mathbf{M}_{2f} + \mathbf{L}_f + \mathbf{M}_{bf}\right)$

and $\boldsymbol{F}_{pf} = \frac{\mathbf{M}_{1f}}{\Delta t}{}^n\bar{\boldsymbol{p}}_f + \frac{\mathbf{M}_{2f}}{\Delta t^2}\left({}^n\bar{\boldsymbol{p}}_f + {}^n\dot{\bar{\boldsymbol{p}}}_f\Delta t\right) + \mathbf{Q}^T\ \bar{\mathbf{v}}^{i+1}_f + \mathbf{f}_{pf}$

5. Compute the updated stress measures:

${}^{n+1}\boldsymbol{\sigma}'^{i+1}_f = 2\mu\boldsymbol{d}'_f(\bar{\boldsymbol{v}}^{i+1}_f) \quad \rightarrow \quad {}^{n+1}\boldsymbol{\sigma}^{i+1}_f = {}^{n+1}\boldsymbol{\sigma}'^{i+1}_f + {}^{n+1}p^{i+1}_f\boldsymbol{I}$

${}^{n+1}\boldsymbol{\sigma}^{\triangledown,i+1}_s = \boldsymbol{c}^{\sigma J} : \boldsymbol{d}_s\left(\bar{\boldsymbol{v}}^{i+1}_s\right) \quad \rightarrow \quad {}^{n+1}\boldsymbol{\sigma}^{i+1}_s = {}^n\hat{\boldsymbol{\sigma}}_s + \Delta t\ {}^{n+1}\boldsymbol{\sigma}^{\triangledown,i+1}_s$

6. Check the convergence: $\parallel \boldsymbol{R}^{i+1}_{s,f}(\bar{\boldsymbol{v}}^{i+1}_{s,f}, \bar{\boldsymbol{p}}^{i+1}_f) \parallel < tolerance$

If condition 6 is not fulfilled, return to 1 with $i \leftarrow i+1$.

At the end of each time step, for solid elements compute

${}^{n+1}\hat{\boldsymbol{\sigma}}_s = {}^{n+1}\boldsymbol{\sigma}_s + \Delta t\boldsymbol{\Omega}_s\ ({}^{n+1}\bar{\boldsymbol{v}}_s, {}^{n+1}\boldsymbol{\sigma}_s)$

Algorithm 1: Iterative solution scheme for FSI problem solved with the V-element for solids and the VPS/F-element for fluids.

Algorithm **??** shows the procedure for solving the FSI problem using the VP-element or the VPS/S-element for the solid and the VPS/F-element for the fluid.

As explained before, the solid and the fluid pressures are two different degrees of freedom. As a consequence, the mass balance equations are solved separately for the fluid and the solid. In particular the mass balance equation is solved twice for the interface nodes. All this increases the computational cost of the analysis with respect to the coupling with the V-element described in Algorithm . For the other hand, this scheme is more general becuase it allow us to solve FSI problems where also incompressible solids are involved.

For each iteration i:

1. Compute the nodal velocity increments $\boldsymbol{\Delta\bar{v}}_{s,f}$:

$\boldsymbol{K}^i_{s,f}\boldsymbol{\Delta\bar{v}}_{s,f} = \boldsymbol{R}^i_{s,f}(\bar{\boldsymbol{v}}^i_{s,f}, \bar{\boldsymbol{p}}^i_{s,f})$

where for fluids: $\boldsymbol{K}^i_f = \boldsymbol{K}^m(\bar{\boldsymbol{x}}^i, \boldsymbol{c}^{\triangledown\sigma}_{NF}) + \boldsymbol{K}^g(\bar{\boldsymbol{x}}^i, \boldsymbol{\sigma}^i_f) + \boldsymbol{K}^\rho(\bar{\boldsymbol{x}}^i)$

and for solids: $\boldsymbol{K}^i_s = \boldsymbol{K}^m(\bar{\boldsymbol{x}}^i, \boldsymbol{c}^{\sigma J}) + \boldsymbol{K}^g(\bar{\boldsymbol{x}}^i, \boldsymbol{\sigma}^i_s) + \boldsymbol{K}^\rho(\bar{\boldsymbol{x}}^i)$

2. Update the nodal velocities: ${}^{n+1}\bar{\boldsymbol{v}}^{i+1}_{s,f} = {}^{n+1}\bar{\boldsymbol{v}}^i_{s,f} + \boldsymbol{\Delta\bar{v}}_{s,f}$

3. Update the nodal coordinates: ${}^{n+1}\bar{\boldsymbol{x}}^{i+1}_{s,f} = {}^{n+1}\bar{\boldsymbol{x}}^i_{s,f} + \bar{\boldsymbol{u}}_{s,f}(\boldsymbol{\Delta\bar{v}}_{s,f})$

4. Compute the fluid nodal pressures $\bar{\boldsymbol{p}}^{i+1}_f$: $\boldsymbol{H}_f\bar{\boldsymbol{p}}^{i+1}_f = \boldsymbol{F}_{pf}(\bar{\boldsymbol{v}}^{i+1}_f, \bar{\boldsymbol{p}}^i_f)$

where: $\boldsymbol{H}_f = \left(\frac{1}{\Delta t}\mathbf{M}_{1f} + \frac{1}{\Delta t^2}\mathbf{M}_{2f} + \mathbf{L}_f + \mathbf{M}_{bf}\right)$

and $\boldsymbol{F}_{pf} = \frac{\mathbf{M}_{1f}}{\Delta t}{}^n\bar{\boldsymbol{p}}_f + \frac{\mathbf{M}_{2f}}{\Delta t^2}\left({}^n\bar{\boldsymbol{p}}_f + {}^n\bar{\dot{\boldsymbol{p}}}_f\Delta t\right) + \mathbf{Q}^T\,\bar{\mathbf{v}}^{i+1}_f + \mathbf{f}_{pf}$

5. Compute the solid nodal pressures $\bar{\boldsymbol{p}}^{i+1}_s$: $\boldsymbol{H}_s\bar{\boldsymbol{p}}^{i+1}_s = \boldsymbol{F}_{ps}(\bar{\boldsymbol{v}}^{i+1}_s, \bar{\boldsymbol{p}}^i_s)$

where for the VP-element: $\boldsymbol{H}_s = \frac{1}{\Delta t}\mathbf{M}_{1s}$

and $\boldsymbol{F}_{ps} = \mathbf{Q}^T\,{}^{n+1}\bar{\mathbf{v}}^{i+1}_s + \frac{\mathbf{M}_{1s}}{\Delta t}{}^n\bar{\boldsymbol{p}}_s$

for the VPS/S-element: $\boldsymbol{H}_s = \left(\frac{1}{\Delta t}\mathbf{M}_{1s} + \frac{1}{\Delta t^2}\mathbf{M}_{2s} + \mathbf{L}_s + \mathbf{M}_{bs}\right)$

and $\boldsymbol{F}_{ps} = \frac{\mathbf{M}_{1s}}{\Delta t}{}^n\bar{\boldsymbol{p}}_s + \frac{\mathbf{M}_{2s}}{\Delta t^2}\left({}^n\bar{\boldsymbol{p}}_s + {}^n\bar{\dot{\boldsymbol{p}}}_s\Delta t\right) + \mathbf{Q}^T\,\bar{\mathbf{v}}^{i+1}_s + \mathbf{f}_{ps}$

6. Compute the updated stress measures:

${}^{n+1}\boldsymbol{\sigma}'^{i+1}_f = 2\mu\boldsymbol{d}'_f(\bar{\boldsymbol{v}}^{i+1}_f)$; ${}^{n+1}\boldsymbol{\sigma}^{i+1}_f = {}^{n+1}\boldsymbol{\sigma}'^{i+1}_f + {}^{n+1}p^{i+1}_f\boldsymbol{I}$

${}^{n+1}\boldsymbol{\sigma}^{i+1}_s = {}^n\hat{\boldsymbol{\sigma}}_s + {}^{n+1}\bar{p}^{i+1}_s\boldsymbol{I} + 2\mu\Delta t\left[\mathbf{I}' : \boldsymbol{d}_s\left(\bar{\boldsymbol{v}}^{i+1}_s\right)\right]$

7. Check the convergence: $\| \boldsymbol{R}^{i+1}_{s,f}(\bar{\boldsymbol{v}}^{i+1}_{s,f}, \bar{\boldsymbol{p}}^{i+1}_{s,f}) \| < tolerance$

If condition 7 is not fulfilled, return to 1 with $i \leftarrow i+1$.

At the end of each time step, for the solid elements

${}^{n+1}\hat{\boldsymbol{\sigma}}_s = {}^{n+1}\boldsymbol{\sigma}_s + \Delta t\boldsymbol{\Omega}_s\ ({}^{n+1}\bar{\boldsymbol{v}}_s, {}^{n+1}\boldsymbol{\sigma}_s)$

Algorithm 2: Iterative solution scheme for FSI problem solved with the VP or/and the VPS/S element for solids and the VPS/F-element for fluids.

8. Assembly of the global linear system and interface detection

The assembly of the global linear system is performed by making a loop over all the nodes of the mesh. Each node provides the contributions of the elements that share the node and each element is computed according to the specific constitutive law and the solution scheme chosen. So, when an interface node is analyzed, it is necessary to sum the contributions of both materials in the global linear system. Because the fluid and the solid pressures are two different degrees of freedom, the fluid elements assemble only the contributions for the fluid pressure, while the solid elements do that for the solid pressure.

In order to ensure the coupling, the fluid and the solid meshes must have in common the nodes along the interface. In other words, there must be a node to node conformity. This is guaranteed by exploiting the capability of the PFEM for detecting the boundaries [35]. The fluid detects the solid interface nodes in the same way it recognizes its rigid contours. This is performed by an efficient combination between the Alpha Shape method and the Delaunay triangulation [36]. According to this strategy, if the separation of the fluid contour from the solid domain is small enough so that that the Alpha Shape criteria are fulfilled, a fluid element connecting the fluid domain to the solid domain is generated. Otherwise the two domains keep apart from each other.

In Figure 1 a graphic representation of the method for detecting the fluid-solid interface is given.

In the situation described in the pictures of Figures 1a-1c none of the contact elements (the light grey elements of Figure 1b) generated by the Delaunay triangulation fulfill the Alpha Shape criteria. Hence for the forthcoming time step interval there is not interaction between the solid and the fluid domains. Instead, in the sequence illustrated in Figures 1d-1f some hybrid elements that share solid and fluid nodes have been generated. In this case, the coupling is active and the equations assembly for the interface nodes is done as described before.

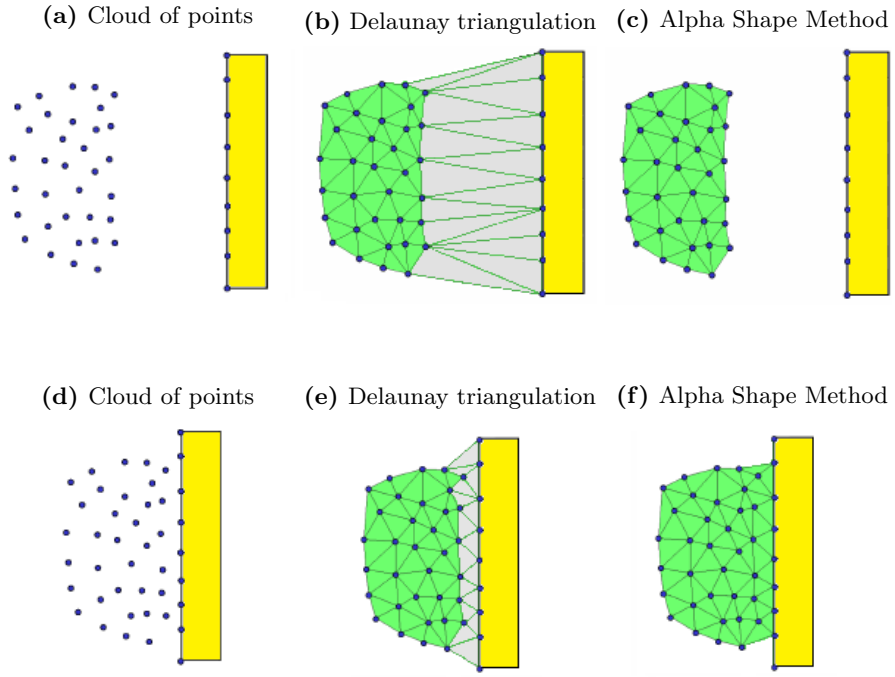

Figure 1: Detection of an interface with the PFEM [37].

9. Numerical examples

We present several examples for validating the Unified formulation. Three FSI problems are presented and the numerical results are compared to the numerical solutions. A comparison between the three solid elements (V, the VP and the VPS/S elements) derived in this work is also given for all the problems presented. In all the numerical examples, the effect of the air has not been taken into account and the VPS/F-element has been used for the fluid parts of the domain. The numerical examples involve large displacements of the solid structures and free surface flows. The combination of these features increases the complexity of the problems.

9.1. Falling of a cylinder in a viscous fluid

The two-dimensional abstraction of the moving of a circular solid cylinder between two parallel walls. The cylinder moves prependicularly to its axis due to the gravity force increasing the falling velocity until an asyntotic value.

The distance from the rigid walls and the axis of the cylinder is $l = 0.02m$. The radius of the circle is $a = 0.0025m$. The geometry of the problem and the material data are given in Figure 2 and Table 2.

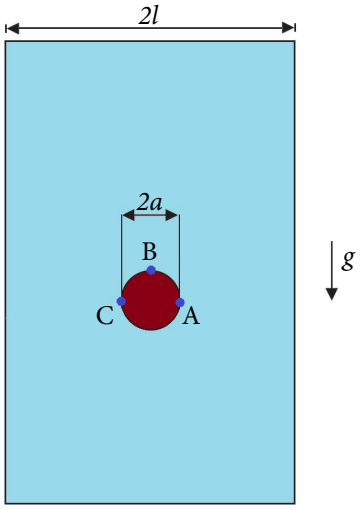

Figure 2: Falling of a cylinder in a viscous fluid. Initial geometry.

Geometric data	
l	$0.02\ m$
a	$0.0025\ m$
g	$9.81\ m/s^2$
Fluid data	
Density	$1.0{\cdot}10^3\ kg/m^3$
Viscosity	$0.1\ Pa \cdot s$
Solid data	
Density	$1.2{\cdot}10^3\ kg/m^3$
Young modulus	$10^7 GPa$
Poisson ratio	0.35

Table 2: Falling of a cylinder in a viscous fluid. Problem data.

The solid cylinder has been modeled not as a quasi-rigid body with an hypoelastic model and a high value for the Young modulus. The VP formulation has been used for the solid.

This numerical example was already studied in other publications [38, 39, 40]. The problem can be also compared to the analytical study of the motion of a rigid cylinder with constant velocity U between two parallel plane walls [41]. For the fluid viscosity $0.1Pa \cdot s$ and slip conditions on the walls, both numerical and analytical strategies give the velocity of fall of the cylinder reaching an asymptotic value of around $U_{max} = 0.0365m/s$.

In this work, the problem has been solved for both stick and slip conditions on the vertical walls of the container.

In Figure 3 the velocity field obtained considering slip boundary conditions is given for three time instants.

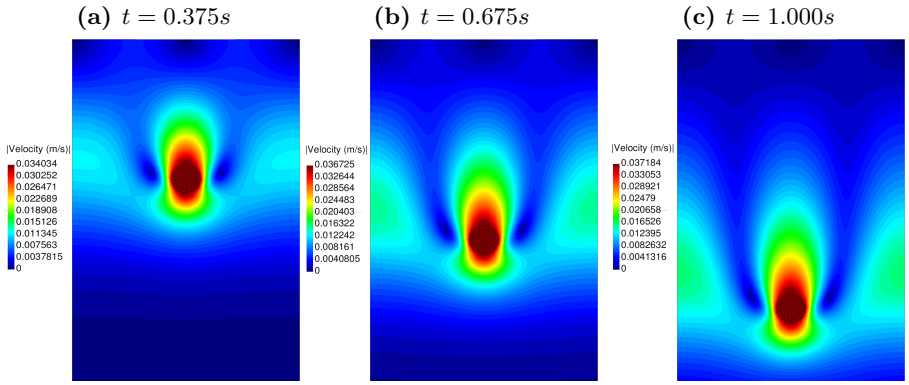

Figure 3: Falling of a cylinder in a viscous fluid. Snapshots of the cylinder motion with velocity contours at different instants of the 2D simulation for the slip case.

In Figure 4, the results for the stick case for the same time instants of Figure 3 are given.

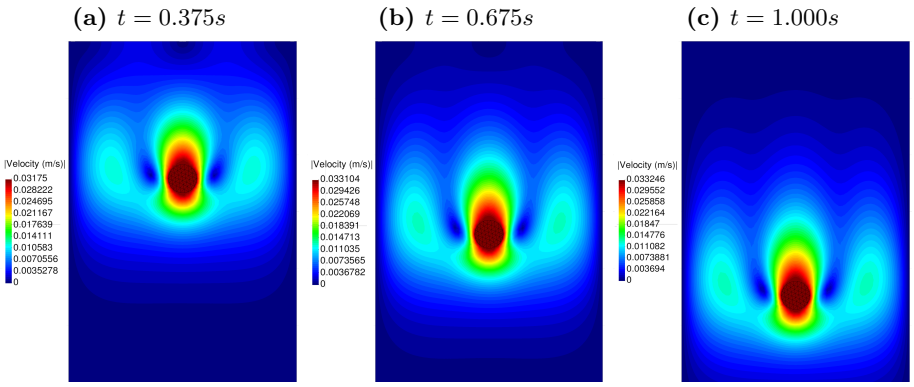

Figure 4: Falling of a cylinder in a viscous fluid. Snapshots of the cylinder motion with velocity contours at different instants of the 2D simulation for the stick case.

The resulting pressure field for the slip and stick cases is illustrated in Figure

5. The pictures show that the perturbation over the fluid pressure field caused by

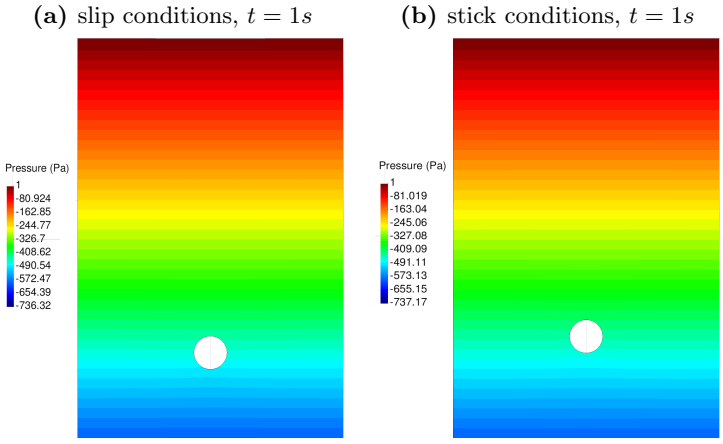

Figure 5: Falling of a cylinder in a viscous fluid. Pressure field obtained for the slip and stick cases.

the motion of the cylinder is almost imperceptible and there are not significant differences between the slip and stick cases.

In the graph of Figure 6 the time evolution of the vertical velocity of the cylinder obtained with the finest mesh (average size=$0.0004m$) are given for both the slip and stick cases.

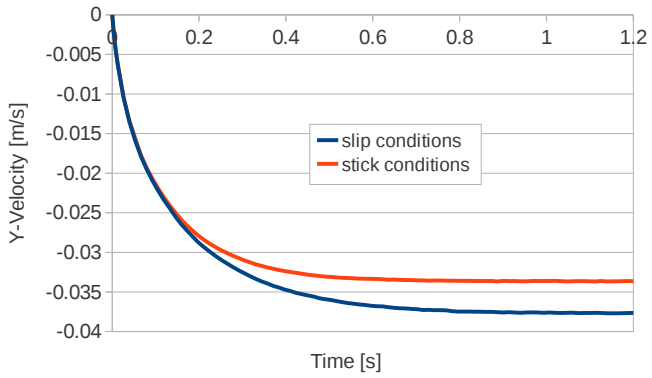

Figure 6: Falling of a cylinder in a viscous fluid. Time evolution of the vertical velocity of the cylinder. Results for the slip and stick cases.

The terminal velocities of the cylinder obtained for the slip and the stick cases are $0.0377m/s$ and $0.0336m/s$, respectively.

For this example the transmission conditions between the solid and the fluid domain have been monitored. The curves of Figure 7 represent the time evolution of the Neumann condition in the X-direction (horizontal) at the points A, B, C located at the boundary of the cylinder and depicted in Figure 2. Specifically, the value plotted in the curves is the mean value of the X-component of vector $\boldsymbol{\sigma n}$ $(\sigma_{xx}n_x + \tau_{xy}n_y)$ computed for the fluid and the solid elements at the points A, B, C of Figure 2.

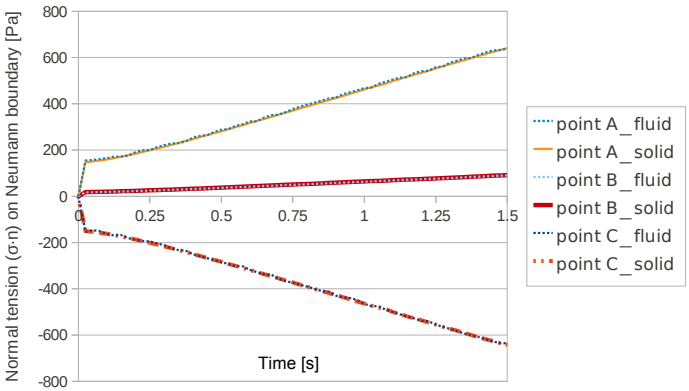

Figure 7: Falling of a cylinder in a viscous fluid. Time evolution of the X-component of $\sigma_{xx}n_x + \sigma_{xy}n_y$ computed at the point A, B, C of Figure 2.

The graph shows that the transmission condition is guaranteed during all the analysis.

The problem has been solved also for a quasi-incompressible solid. For this case a Poisson ratio of 0.4999 and the same Young modulus of the previous case have been considered. The simulation has been run considering stick conditions on the walls and using a mean mesh size of $0.007m$, as for the problem plotted in Figure 4. In Figure 8 the velocity and the pressure fields for the solid and the fluid computed at $t = 1s$ are given.

In the graph of Figure 9 the time evolution of the vertical velocity obtained with the VPS/S-element for $\nu = 0.4999$ is compared with the solution obtained

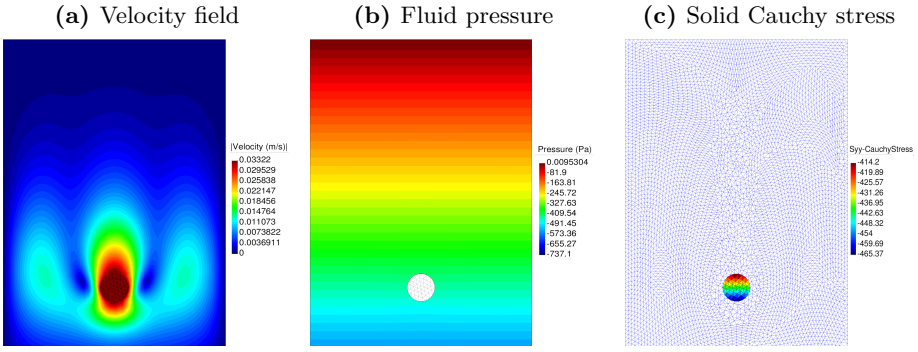

Figure 8: Falling of a cylinder in a viscous fluid. Quasi-incompressible solid ($\nu = 0.4999$). Velocity and the pressure fields and solid Cauchy stress (YY-component) at $t = 1s$ for stick conditions on the walls and a mean mesh size of $0.007m$.

with the VP-element for $\nu = 0.35$ and the same average mesh size and boundary conditions.

As expected, the solutions are almost the same and the vicinity to the incompressible limit does not compromise the quality of the results.

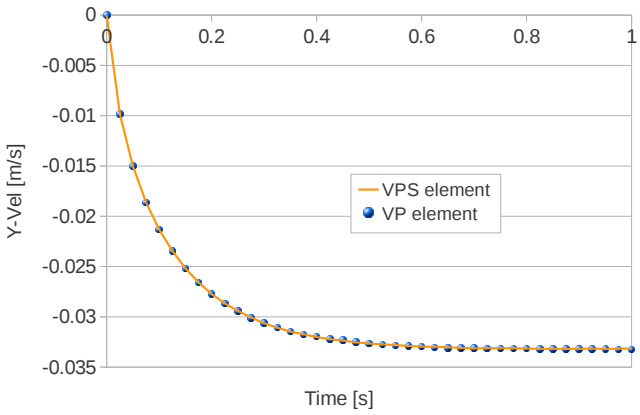

Figure 9: Falling of a cylinder in a viscous fluid. Solutions obtained with two different elements for the solid: the VP-element ($\nu = 0.35$) and the VPS/S-element ($\nu = 0.4999$).

9.2. Filling of an elastic container with a viscous fluid

This example is inspired from a similar problem presented in [37]. A volume of a viscous fluid drops from a rigid container over a thin and highly deformable elastic membrane. The impact of the fluid mass causes an initial huge stretching of the structure and its subsequent oscillations. Two horizontal rigid walls are placed at the top of the elastic container in order to avoid the leackage of the fluid. The problem was solved in 2D for two different values of the fluid viscosity, namely 50 and 100 $Pa \cdot s$. For the structure, both the V and VP elements presented in this work have been used. The purpose was to compare the formulations and to show that both solid elements can be used for the modeling of standard elastic solids in FSI problems. The initial geometry of the problem is given in Figure 3 and the material data are given in Table 3.

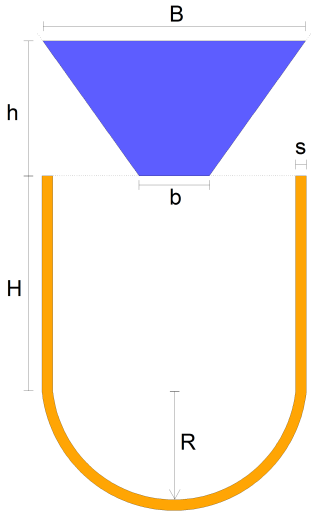

Figure 10: Filling of an elastic container with a viscous fluid. Initial geometry.

Geometry data	
h	2.5
H	3.75
R	2.25
b	1.3
B	4.8714
s	0.2
Fluid data	
Viscosity	$50, 100\ Pa \cdot s$
Density	$1000\ kg/m^3$
Solid data	
Young modulus	$2.1\ 10^7 GPa$
Poisson ratio	0.3
Density	$20\ kg/m^3$

Table 3: Filling of an elastic container with a viscous fluid. Problem data.

In the graph of Figure 11 the results for the less viscous case (μ=50 Pa·s) obtained using the V and the VP elements are given. The comparison is performed for the vertical displacement of the lowest point of the elastic structure.

The curves are almost coincident and only after $4.5s$ of simulation some slight

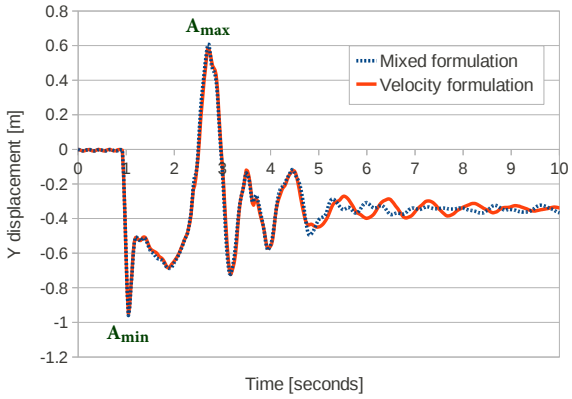

Figure 11: Filling of an elastic container with a viscous fluid ($\mu = 50Pa \cdot s$). Vertical displacement of the bottom of the container obtained using the V and the VP elements for the solid domain.

differences appear.

In Table 4 the maximum and the minimum vertical displacements of the elastic structure obtained with the V and the VP elements are collected. A_{min} and A_{max} refer to the minimum and maximum points of the curves of Figure 11. The numerical results obtained with the two solid elements are very close.

Point	V-element		VP-element	
	time instant	vertical disp.	time instant	vertical disp.
A_{min}	1.045 s	-0.951 m	1.045 s	-0.961 m
A_{max}	2.695 s	0.586 m	2.695 s	0.606 m

Table 4: Filling of an elastic container with a viscous fluid ($\mu = 50Pa \cdot s$). Maximum and minimum vertical displacements for the V and the VP elements.

For the same problem, some representative snapshots are collected in Figure 12. Over the solid domain the pressure contours are depicted and over the fluid one the mesh is plotted. The numerical results correspond to the simulation using the VP-element for the solid.

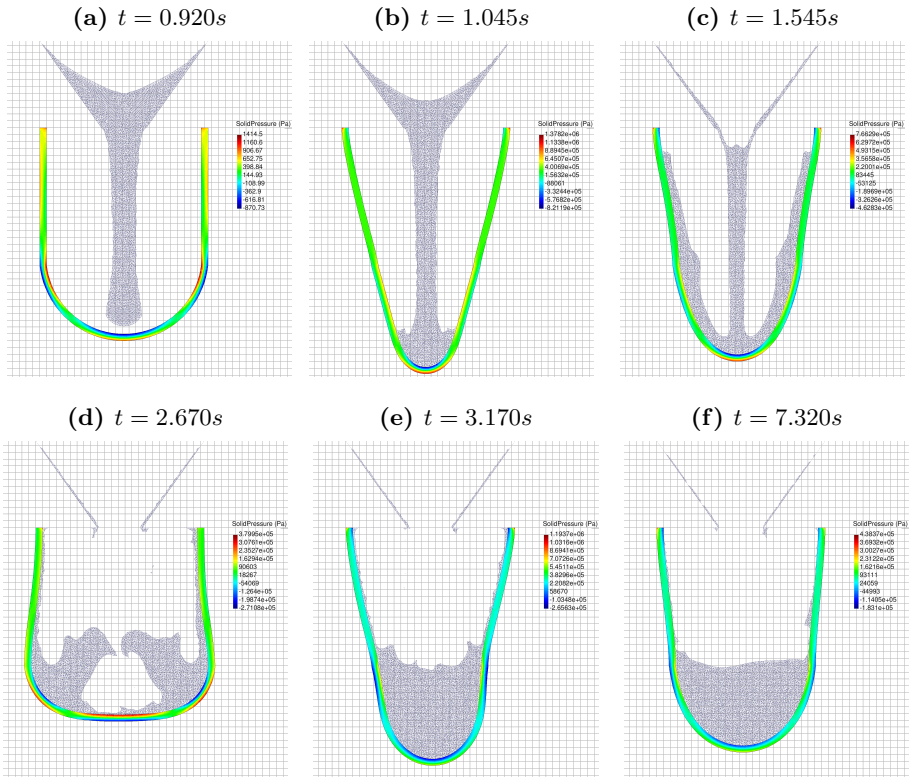

Figure 12: Filling of an elastic container with a viscous fluid ($\mu = 50Pa{\cdot}s$). Snapshots of the numerical simulation at different instants. Pressure contours are depicted over the solid domain.

In Figure 13 snapshots of the numerical simulation for the most viscous case (μ=100 Pa·s) are given for the same time instants of Figure 12. The numerical results correspond again to the solution obtained using the VP-element for the solid domain.

The results obtained with the V and VP elements are compared for the most viscous case analyzing the time evolution of the vertical displacement at the bottom of the container. In Figure 14 the solutions obtained using both elements are plotted.

Once again, the differences between the results of the two formulations for

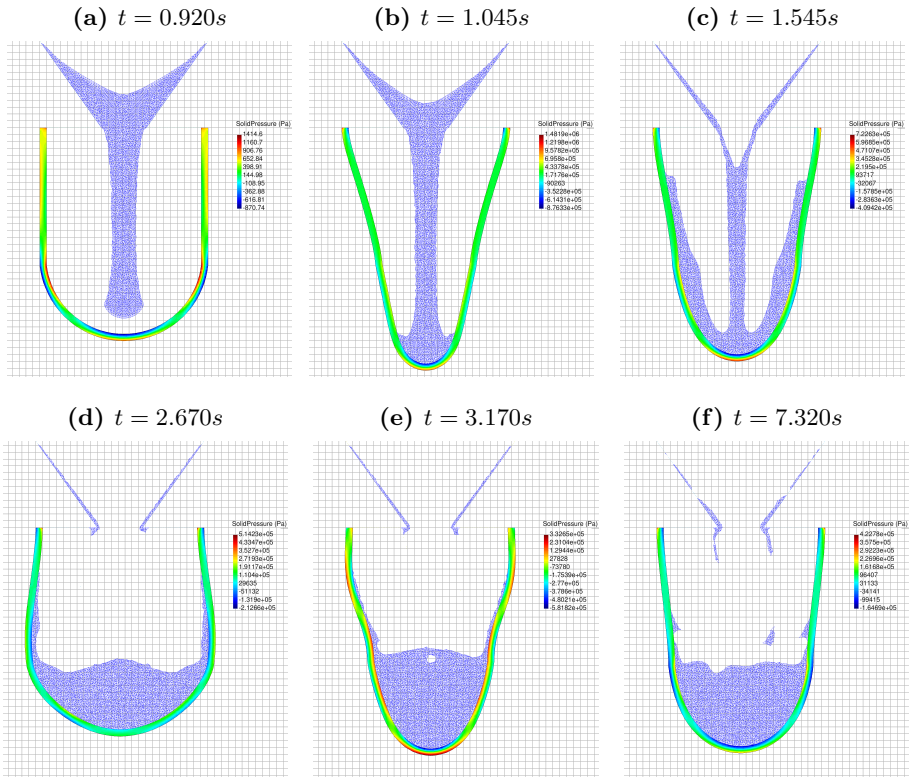

Figure 13: Filling of an elastic container with a viscous fluid ($\mu = 100Pa \cdot s$). Snapshots at different instants of the 2D simulation. Pressure contours depicted over the solid domain.

the solid are very small. This is a further evidence of the validity and flexibility of the unified formulation, that allow us to choose for the solid either a velocity or a mixed formulation.

The maximum and the minimum vertical displacements of the structure obtained by the V and the VP elements are collected in Table 5. B_{min} and B_{max} correspond to the points of the graph marked in Figure 14.

Comparing the results of Tables 4 and 5, one may note that the lowest position of the structure is almost the same for both problems, although in the most viscous case it is reached slightly later. For the maximum upward

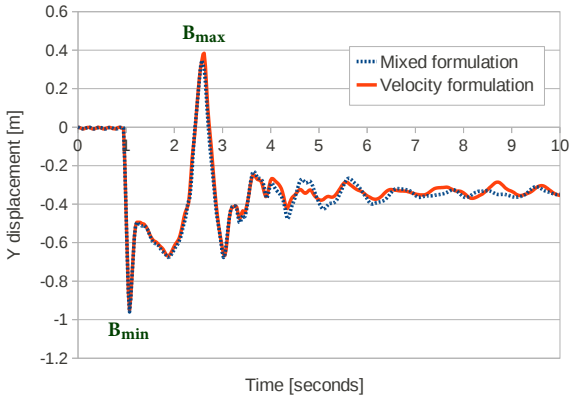

Figure 14: Filling of an elastic container with a viscous fluid ($\mu = 100Pa \cdot s$). Vertical displacement of the bottom of the elastic container obtained using the V and the VP elements for the solid domain.

Point	V-element		VP-element	
	time instant	vertical disp.	time instant	vertical disp.
B_{min}	1.070 s	-0.950 m	1.070 s	-0.960 m
B_{max}	2.620 s	0.384 m	2.570 s	0.347 m

Table 5: Filling of an elastic container with a viscous fluid ($\mu = 100Pa \cdot s$). Maximum and minimum vertical displacements for the V and the VP elements.

displacement, the differences between the two problems are bigger. In fact, the maximum upward displacement of the container is significally larger for the less viscous fluid and the highest position is reached later. This because the less viscous fluid splashes more and moves away from the bottom of the elastic container reducing the weight acting over the container walls.

9.3. Collapse of a water column on a deformable membrane

The problem illustrated in Figure 15 was introduced by Walhorn *et al.* [42].

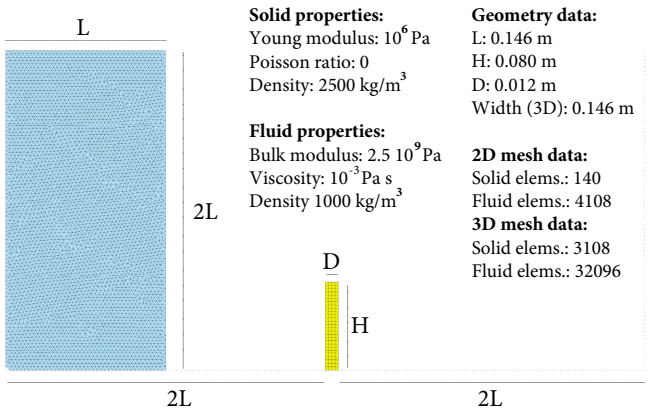

Figure 15: Collapse of a water column on a deformable membrane. Initial geometry and problem data.

The water column collapses by instantaneously removing the vertical wall. This originates the flow of water within the tank, the formation of a jet after the water stream hits the ground, and the subsequent sloshing of the fluid as it impacts a highly deformable elastic membrane. The membrane bends and starts oscillating under the effect of its inertial forces and the impact with the water stream.

In Figure 16 some representative snapshots of the 2D simulation are given. The VP-element for the solid was used for the analysis.

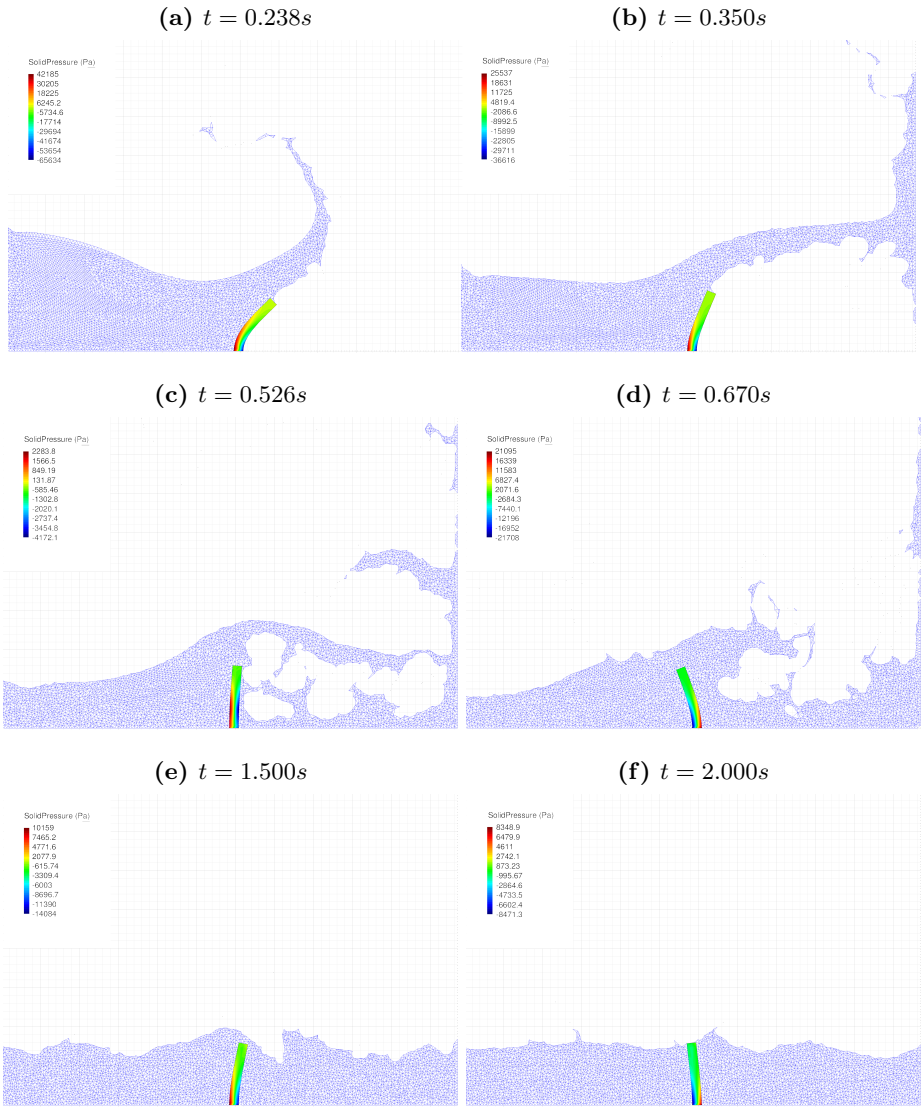

Figure 16: Collapse of a water column on a deformable membrane. Snapshots of the 2D simulation at different instants. The VP-element is used for the solid.

The results obtained with the present formulation using the V-element and the VP-element for the solid have been compared to the ones computed in [43, 44, 37]. In the graph of Figure 17 the time evolution of the horizontal deflection of the left top corner is illustrated.

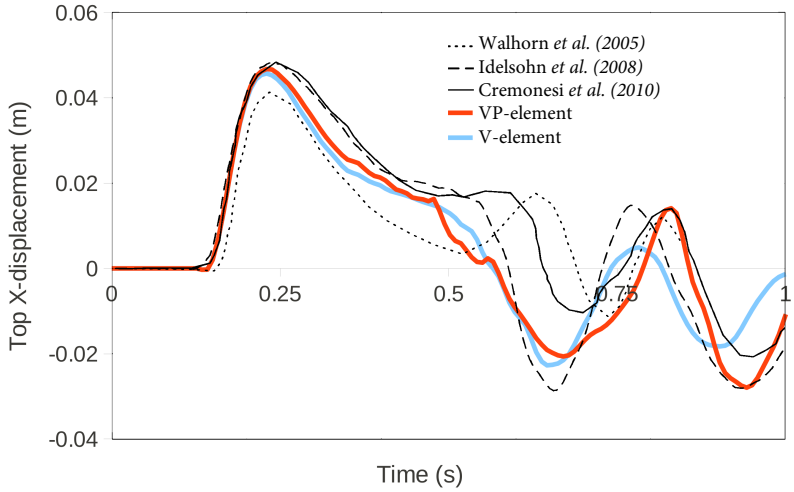

Figure 17: Collapse of a water column on a deformable membrane. Horizontal deflection of the left top corner on time. Numerical results obtained with the V and VP elements for the solid. Comparison with numerical results obtained in [42, 44, 37].

The diagram shows that, for the first part of the analysis, the proposed formulation agrees well with the results reported in the literature. After around $0.5s$ of simulation, the numerical results of each formulation starts to diverge, although for all the formulations the membrane oscillates two times around its vertical position before the time instant $t = 1s$.

The first part of the simulation is easier to analyze than the second one because the phenomena to model are less aleatory and the fluid splashes do not affect the results, as it occurs in the second part of the simulation. Furthermore, the differences between the numerical simulations accumulate throughout the analysis. In other words, even a slight difference in the first part of the simulation may produce a huge variation of the results for the rest part of the analysis. In fact, the inital deformation of the elastic structure affects highly

the rest of the simulation: a smaller bending of the membrane induces an impact of the water stream at an higher height of the containing wall and with a bigger tangential component of the impact velocity. Consequently, the fluid stream impacts against the right side of the elastic membrane later and with reduced inertial forces. These considerations have an even greater effect for 3D simulations.

The same example has been solved also in 3D, considering a width of $0.148m$ for the prismatic tank. In order to maintain the plane strain state of the 2D problem, in the 3D analysis the nodal displacements of the elastic membrane in the transversal direction to the impact velocity of the water stream have been constrained. The mesh data of the 3D problem are given in Figure 15. For the 3D simulation of the problem the V-element has been used for the solid.

In Figure 18 the numerical results of the 3D simulation are given.

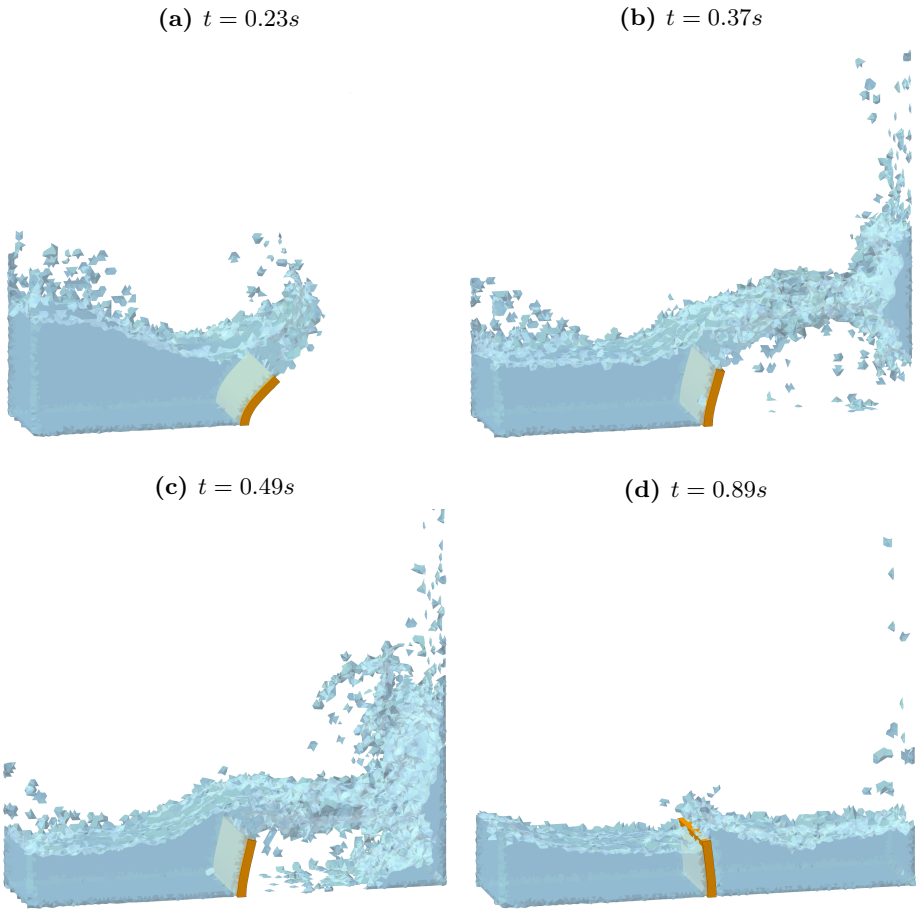

Figure 18: Collapse of a water column on a deformable membrane. Snapshots of the 3D simulation of different instants. The V-element is used for the solid.

No numerical or experimental results have been found in the literature for the described 3D abstraction of the 2D benchmark problem presented in [42]. For this reason, 3D results have been compared only to the analogous 2D problem. Figure 19 shows the time evolution of the 2D and 3D results for the horizontal deflection of the left top corner obtained with the V-element. For the reasons explained before, the comparison between the 2D and the 3D results is given only for the first $0.5s$ of the analysis.

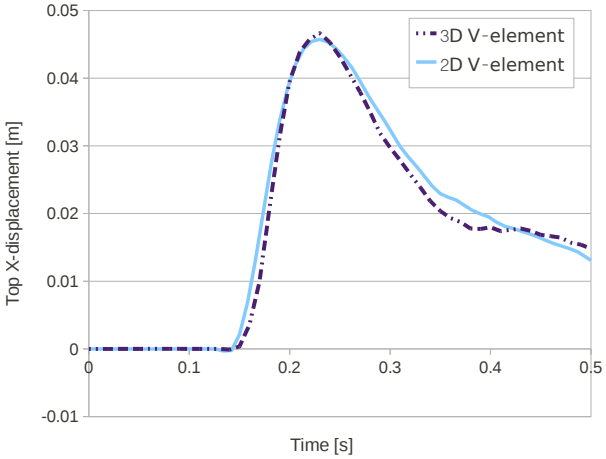

Figure 19: Collapse of a water column on a deformable membrane. Horizontal deflection of the left top corner on time. Comparison between 2D and 3D analyses for the V-element.

Figure 19 shows that the 3D results agree well with the ones of the 2D analysis for the first part of the simulation.

In order to facilitate future comparisons, in Figure 20 the time variation of the horizontal deflection of the left top corner of the 3D simulation is given for the same duration of the 2D analysis, *i.e.* $1s$.

Clearly, aspects such as mesh refinement and a larger definition of the width of the analysis domain will affect the PFEM results in the interval $0.5s$-$1s$.

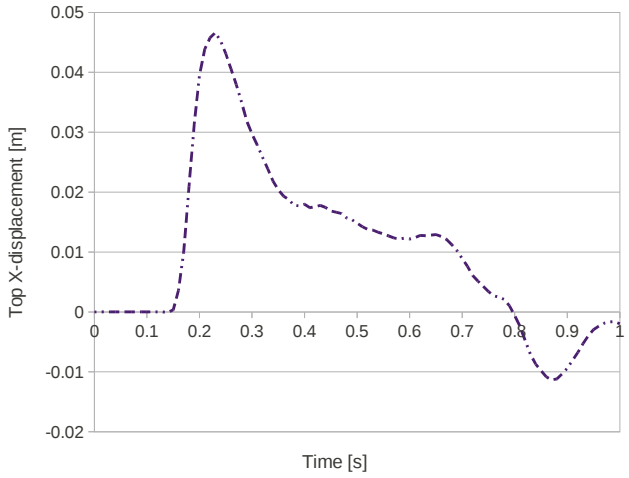

Figure 20: Collapse of a water column on a deformable membrane (3D simulation). Time evolution of the horizontal deflection of the left top corner. Results obtained with the V-element for the solid.

10. Concluding remarks

In this work, a Unified formulation for fluid and solid mechanics and FSI problems has been presented.

The method is based on a mixed velocity-pressure formulation. For quasi-incompressible materials the numerical simulation is stabilized using the FIC-FEM procedure derived in [1] for Newtonian fluids and applied in this work also for quasi-incompressible hypoelastic solids.

For the solid parts of the domain, three different hypoelastic elements have been presented, namely the V, the VP and the VPS/S elements respectively based on a velocity, mixed velocity-pressure and mixed velocity-pressure stabilized formulation.

The Unified formulation, through an efficient combination of the PFEM for the fluid, and the FEM for the solid, allow us to solve FSI problems in a monolithic way ensuring automatically a strong coupling. Furthermore, the risk of ill-conditioning in the global linear system of algebraic equations is reduced using the same unknown variables for the fluid and the solid and solving the global problem through a partitioned a scheme.

The efficiency of the method has been tested by solving FSI becnhmark problems, involving free surface viscous flows and large displacements for the solid structure. Good agreement between the results obtained by the present formulation and published results has been found in all cases for all the solid elements derived in this work.

References

[1] E. Oñate, A. Franci, J. Carbonell, Lagrangian formulation for finite element analysis of quasi-incompressible fluids with reduced mass losses, International Journal for Numerical Methods in Fluids 74 (10) (2014) 699–731.

[2] F. Brezzi, On the existence, uniqueness and approximation of saddle-point problems arising from lagrange multipliers, Revue française d'automatique, informatique, recherche opérationnelle. Série rouge. Analyse numérique 8(R-2) (1974) 129–151.

[3] F. Felippa, E. Oñate, Nodally exact ritz discretizations of 1d diffusion-absorption and helmholtz equations by variational fic and modified equation methods, Computational Mechanics 39 (2007) 91–111.

[4] E. Oñate, Derivation of stabilized equations for advective-diffusive transport and fluid flow problems, Computer methods in applied mechanics and engineering 151 (1998) 233–267.

[5] E. Oñate, A. Valls, J. García, Fic/fem formulation with matrix stabilizing terms for incompressible flows at low and high reynold's numbers., Computational mechanics 38 (4-5) (2006) 440–455.

[6] E. Oñate, J. García, S. Idelsohn, F. D. Pin, Fic formulations for finite element analysis of incompressible flows. eulerian, ale and lagrangian approaches., Computer methods in applied mechanics and engineering 195 (23-24) (2006) 3001–3037.

[7] E. Oñate, P. Nadukandi, S. Idelsohn, J. García, C. Felippa, A family of residual-based stabilized finite element methods for stokes flows, International Journal for Numerical Methods in Fluids 65(1-3) (2011) 106–134.

[8] E. Oñate, I. SR, F. C, Consistent pressure laplacian stabilization for incompressible continua via higher-order finite calculus, International Journal of Numerical Methods in Engineering 87(1:5) (2011) 171–195.

[9] O. Zienkiewicz, R. Taylor, The Finite Element Method. Its Basis and Fundamentals. (6th Ed.), Elsevier Butterworth-Heinemann, Oxford, 2005.

[10] S. Idelsohn, E. Oñate, F. D. Pin, The particle finite element method: a powerful tool to solve incompressible flows with free-surfaces and breaking waves, International Journal for Numerical Methods in Engineering 61 (2004) 964–989.

[11] H. Edelsbrunner, E. Mucke, Three dimensional alpha shapes, ACM Trans Graphics 13 (1999) 43–72.

[12] A. Larese, R. Rossi, E. Oñate, S. Idelsohn, Validation of the particle finite element method (pfem) for simulation of free surface flows, International Journal for Computer-Aided Engineering and Software 25 (2008) 385–425.

[13] M. Cremonesi, L. Ferrara, A. Frangi, U. Perego, A lagrangian finite element approach for the simulation of water-waves induced by landslides, Computer and Structures 89 (2011) 1086–1093.

[14] B. Tang, J. Li, T. Wang, Some improvements on free surface simulation by the particle finite element method, International Journal for Numerical Methods in Fluids 60 (9) (2009) 1032–1054.

[15] R. Aubry, S. R. Idelsohn, E. Oñate, Particle finite element method in fluid-mechanics including thermal convection-diffusion, Computers and Structures 83 (2005) 1459–1475.

[16] E. Oñate, R. Rossi, S. Idelsohn, K. Butler, Melting and spread of polymers in fire with the particle finite element method., International Journal of Numerical Methods in Engineering 81 (8) (2010) 1046–1072.

[17] E. Oñate, A. Franci, J. Carbonell, A particle finite element method (pfem) for coupled thermal analysis of quasi and fully incompressible flows and fluid-structure interaction problems, Numerical Simulations of Coupled Problems in Engineering. S.R. Idelsohn (Ed.) 33 (2014) 129–156.

[18] S. Idelsohn, J. Marti, P. Becker, E. Oñate, Analysis of multifluid flows with large time steps using the particle finite element method, International Journal for Numerical Methods in Engineering 75 (9) (2014) 621–644.

[19] T. Dang, G. Meschke, An ale-pfem method for the numerical simuation of two-phase mixture flow, Computer Methods in Applied Mechanics and Engineering 278 (2014) 599–620.

[20] X. Zhang, K. Krabbenhoft, D. Sheng, Particle finite element analysis of the granular column collapse problem, Granular Matter 16 (2014) 609–619.

[21] E. Oñate, S. Idelsohn, M. Celigueta, R. Rossi, Advances in the particle finite element method for the analysis of fluid–multibody interaction and bed erosion in free surface flows, Computer methods in applied mechanics and engineering 197 (19-20) (2008) 1777–1800.

[22] E. Oñate, M. Celigueta, S. Idelsohn, F. Salazar, B. Suarez, Possibilities of the particle finite element method for fluid–soil–structure interaction problems, Computation mechanics 48 (2011) 307–318.

[23] M. Zhu, M. H. Scott, Modeling fluid-structure interaction by the particle finite element method in opensees, Computers and Structures 132 (2014) 12–21.

[24] J. Carbonell, E. Oñate, B. Suarez, Modeling of ground excavation with the particle finite-element method, Journal of Engineering Mechanics 136 (2010) 455–463.

[25] J. Carbonell, E. Oñate, B. Suarez, Modelling of tunnelling processes and cutting tool wear with the particle finite element method (pfem), Computational Mechanics 52 (3) (2013) 607–629.

[26] E. Oñate, A. Franci, J. Carbonell, A particle finite element method for analysis of industrial forming processes, Computational Mechanics 54 (2014) 85–107.

[27] E. Oñate, J. Carbonell, Updated lagrangian finite element formulation for quasi and fully incompressible fluids, Computational Mechanics 54 (6).

[28] P. Becker, S. Idelsohn, E. Oñate, A unified monolithic approach for multi-fluid flows and fluid–structure interaction using the particle finite element method with fixed mesh, Computational Mechanics 61 (2015) 1–14.

[29] C. Truesdell, Hypo-elasticity, Journal of Rational Mechanics and Analysis 4,1.

[30] T. Belytschko, W. Liu, B. Moran, K. Elkhodadry, Nonlinear Finite Elements For Continua And Structures. Second Edition., John Wiley & Sons, New York, 2014.

[31] P. Ryzhakov, E. Oñate, S. Idelsohn, Improving mass conservation in simulation of incompressible flows, International Journal of Numerical Methods in Engineering 90 (2012) 1435–1451.

[32] P. Ryzhakov, R. Rossi, S. Idelsohn, E. Oñate, A monolithic lagrangian approach for fluid-structure interaction problems, Computational Mechanics 46 (2010) 883–899.

[33] P. Ryzhakov, J. Cotela, R. Rossi, E. Oñate, A two-step monolithic method for the efficient simulation of incompressible flows, International Journal for Numerical Methods in Fluids 74 (12) (2014) 919–934.

[34] A. Franci, E. Oñate, J. Carbonell, On the effect of the bulk tangent matrix in partitioned solution schemes for nearly incompressible fluids, International Journal for Numerical Methods in Engineering DOI: 10.1002/nme.4839.

[35] E. Oñate, S. Idelsohn, F. D. Pin, R. Aubry, The particle finite element method. an overview, International Journal for Computational Methods 1 (2004) 267–307.

[36] S. Idelsohn, N. Calvo, E. Oñate, Polyhedrization of an arbitrary point set, Computer Methods in Applied Mechanics and Engineering 92 (22–24) (2003) 2649–2668.

[37] M. Cremonesi, Doctoral thesis: A Lagrangian Finite Element Method for the Interaction Between Flexible Structures and Free Surfaces Fluid Flows, 2010.

[38] A. Gil, A. A. Carreño, J. Bonet, O.Hassan, The immersed structural potential method for haemodynamic applications, Journal of Computational Physics 229 (2010) 8613–8641.

[39] C. Hesch, A. Gil, A. A. Carreño, J. Bonet, On continuum immersed strategies for fluid–structure interaction, Computer Methods in Applied Mechanics and Engineering 247 (2012) 51–64.

[40] X. Wang, W. Liu, Extended immersed boundary method using fem and rkpm, Computer Methods in Applied Mechanics and Engineering 193 (2004) 1305–1321.

[41] J. Happel, H. Brenner, Low reynolds number hydrodynamics.

[42] E. Walhorn, A. Kolke, B. Hubner, D.Dinkler, Fluid-structure coupling within a monolithic model involving free surface flows, Computer & Structures Methods in Applied Mechanics and Engineering 83 (25-26) (2005) 2100–2111.

[43] B. Hubner, E. Walhorn, D.Dinkler, A monolithic approach to fluid-structure interaction using space-time finite elements, Computer Methods in Applied Mechanics and Engineering 193 (2004) 2087–2104.

[44] S. Idelsohn, J. Marti, A. Limache, E. Oñate, Unified lagrangian formulation for elastic solids and incompressible fluids: Applications to fluid-structure interaction problems via the pfem, Computer Methods In Applied Mechanics And Engineering 197 (2008) 1762–1776.